Entrainment of sediment particles by retrograde vortices: Test of hypothesis using near-particle observations

Fu-Chun Wu[1,2] and Wu-Rong Shih[1]

Received 10 October 2011; revised 28 June 2012; accepted 29 June 2012; published 15 August 2012.

[1] We conduct an experimental study to test the hypothesis that particle entrainment is associated with a passing retrograde vortex (spanwise vortex rotating counter to the mean shear). The pre- and post-entrainment quadrant structures are probed with the laser Doppler velocimetry (LDV) at a near-particle measurement spot, using the shifted-time cumulative quadrant fraction approach. The results are characterized by a pre-entrainment spiky rise of the Q1 fraction (outward interactions) and a mild increase of the Q4 fraction (sweeps), followed by the post-entrainment dominance of the Q4 fraction and a drastic drop of the Q1 fraction. Such results suggest that it is highly probable that particle entrainment is a result of the interactions with a passing retrograde-vortex-type coherent structure. The time series of 2-D velocities at the near-particle spot consistently exhibit the short-term peaks present at the time of entrainment. The quadrant signature at an alternative spot one grain diameter upstream of the target particle exhibits a sequence in which the pre-entrainment dominant Q1 fraction is replaced by the Q4 fraction, followed by a post-entrainment peak of the Q4 fraction. The results obtained from these two locations confirm the theoretical predictions, showing that different quadrant signatures would be detected at different spots during the passage of a retrograde vortex. We also perform an extra set of experiments, in which the target particle is set in an alternative pocket geometry with diagonal downstream valleys. The similar pre-entrainment quadrant signatures detected in all the experiments performed with different types of pocket geometry and the unique post-entrainment quadrant signature detected in those performed with the alternative pocket geometry imply that an obliquely oriented retrograde vortex may have passed, entraining the particle in diagonal directions. The results point to the potential discrepancy in the observed signatures that arises from the misalignment of the velocity measurement plane with the direction of particle entrainment.

Citation: Wu, F.-C., and W.-R. Shih (2012), Entrainment of sediment particles by retrograde vortices: Test of hypothesis using near-particle observations, *J. Geophys. Res.*, *117*, F03018, doi:10.1029/2011JF002242.

1. Introduction

[2] Understanding the role of coherent flow structures in the initiation of sediment motion remains a key challenge for contemporary Earth scientists who seek new insights into the processes of sediment transport and riverbed evolution [*Ferreira*, 2011; *Hardy et al.*, 2011]. Early studies based on the flow visualization techniques have revealed the occurrence of near-bed bursting events [*Kline et al.*, 1967; *Grass*, 1971]. Bursting is a cyclic (but not periodic) flow process characterized by a sequence of lift-up, ejection and sweep motions. These organized motions reflect the passage of an Ω-shaped hairpin vortex or a packet of hairpin vortices (Figure 1) that interact strongly with the near-bed fluid [*Adrian*, 2007]. The three-dimensional (3-D) structures of hairpins would generate in their wakes the streamwise low-speed streaks and induce ejections of low-speed fluid into the outer region of the boundary layer. Ejections are followed by the overpassing sweeps, in which an inrush of higher-speed fluid moving bed-ward would break up the ejected fluid. The passage of a hairpin would also induce a region of adverse (positive) streamwise pressure gradient on the boundary layer, causing localized separations and lift-ups of near-bed fluid. The lifted fluid is subsequently rolled up, leading to the formation of a secondary hairpin. With these autogeneration mechanism and continuing cycles of bursting, new vortices are regenerated such that the near-bed turbulence is sustained [*Smith et al.*, 1991; *Adrian et al.*, 2000].

[3] In gravel bed rivers with complex, porous and irregular surfaces, flows are typically shallow and the relative submergence (the ratio of mean flow depth to roughness height)

[1]Department of Bioenvironmental Systems Engineering, National Taiwan University, Taipei, Taiwan.
[2]Hydrotech Research Institute, National Taiwan University, Taipei, Taiwan.

Corresponding author: F.-C. Wu, Department of Bioenvironmental Systems Engineering, National Taiwan University, Roosevelt Rd., Taipei 10617, Taiwan. (fcwu@ntu.edu.tw)

0148-0227/12/2011JF002242

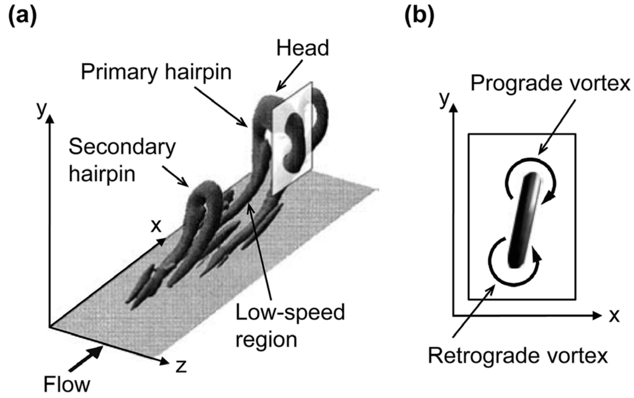

Figure 1. (a) Three-dimensional visualization of a hairpin vortex packet, showing the Ω-shaped hairpin structures and low-speed streaks in their wakes (modified from *Natrajan et al.* [2007]). (b) Spatial signature of retrograde-prograde vortex pair revealed when a hairpin is sliced through its shoulder by a streamwise-vertical (x-y) measurement plane.

seldom exceeds 10 during floods and can be <5 during low flow conditions [*Hardy et al.*, 2009]. In such flows with relatively high roughness, the microtopographies of the bed exert a significant influence on the generation, evolution, and dissipation of coherent structures. Recent experimental studies have shown that the coherent flow structures over gravel beds appear to originate from the bed-generated turbulence, and large-scale outer layer structures are the result of flow-topography interactions in the near-bed region associated with wake flapping [*Hardy et al.*, 2009, 2010].

[4] To detect bursting, researchers in the 1970s have made point velocity measurements at turbulence-resolving frequencies using the techniques such as thermal anemometry or laser Doppler velocimetry (LDV), and employed a conditional sampling and quadrant analysis of streamwise and vertical velocity fluctuations (u', v') to identify the four types of bursting motions, namely, outward interactions (Q1), ejections (Q2), inward interactions (Q3), and sweeps (Q4) [*Wallace et al.*, 1972; *Willmarth and Lu*, 1972]. Quadrant analysis of this kind does not explain the form of the vortices creating bursting motions; it does provide an unambiguous criterion allowing for evaluation of the contributions these motions make to the transport of sediment. For example, using synchronized high-frequency velocimetry and high-speed photography or a coupled system of high-frequency anemometer and sediment flux sensors [e.g., *Nelson et al.*, 1995; *Sterk et al.*, 1998], the instantaneous fluid motions corresponding to the detected sediment transport events can be identified, based on which the fractional contributions of the Q1∼Q4 to sediment entrainment can be evaluated.

[5] A majority of researchers have documented that sweeps (Q4) and ejections (Q2) are the primary contributors to sediment entrainment [*Grass*, 1970, 1974; *Sumer and Deigaard*, 1981; *Best*, 1992; *Niño and Garcia*, 1996; *Sechet and le Guennec*, 1999; *Hurther and Lemmin*, 2003; among others], reasoning that ejections and sweeps account for >60% of all near-bed bursting motions and are the two quadrants that contribute positively to the Reynolds stress $-u'v'$. Another school of researchers, however, have presented laboratory or field evidence supporting the close correlation between the instantaneous sediment flux and instantaneous streamwise velocity u, suggesting that only sweeps (Q4) and outward interactions (Q1) play a significant role in the entrainment and transport of sediment (Figure 2a), since these motions are associated with positive u' and thus greater streamwise velocities [*Thorne et al.*, 1989; *Nelson et al.*, 1995; *Sterk et al.*, 1998; *Weaver and Wiggs*, 2008; among others].

[6] To close such a debate over which bursting motions are really responsible for sediment entrainment is unlikely if one overlooks the convective nature of 3-D vortex structures, not to mention the complexities added by the mixed-size sediment [*Wu and Jiang*, 2007]. Using point measurements and quadrant analyses to detect the coherent structures induced by the convecting and deforming hairpin vortices is indeed questionable, as many regions that exhibit Q2 (ejections) and Q4 (sweeps) show no evidence of notable vortices [*Lu and Smith*, 1991]. Moreover, the chaotic motions of background turbulence and the random bursting phases of coherent motions superimposed in the flowfield would degrade seriously the conditionally averaged spatial and temporal correlations [*Nezu and Nakagawa*, 1993], rendering detection of the true, vortex-induced bursting motions extremely difficult even with the aid of the VITA (variable interval time

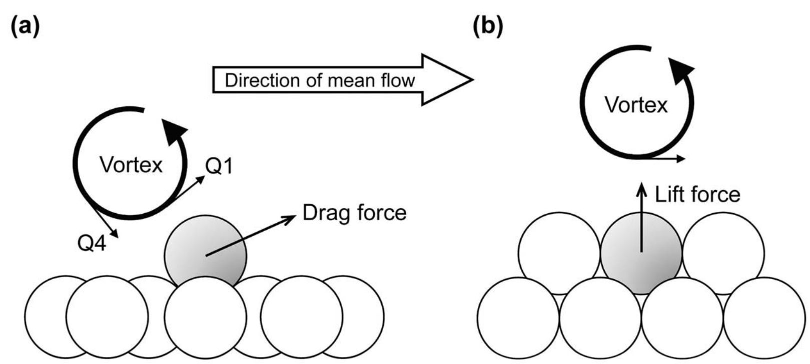

Figure 2. (a) An exposed particle entrained by a retrograde vortex. A drag force is exerted on the particle in the direction of local vortical motions, in the sense of Q1 (outward interactions) followed by Q4 (sweeps). (b) A sheltered particle entrained by a retrograde vortex, resulting from a lift force (net upward pressure) induced by local vortical motions.

average) and pattern-recognition techniques [*Blackwelder and Kaplan*, 1976; *Wallace et al.*, 1977].

[7] Such difficulties have been recently overcome by advances in the particle image velocimetry (PIV) technology. For example, *Hofland and Booij* [2004] used the 2-D PIV in a streamwise-vertical (x-y) plane to identify the coherent structures responsible for entrainment of the target gravel. The conditionally averaged instantaneous flowfields during particle entrainment reveal that the small-scale ejections (Q2) associated with spanwise vortices initiate particle uplift and the large-scale sweeps (Q4) further entrain the target particle over its pivot point. *Cameron* [2006] performed 2-D PIV measurements during particle entrainment, in which the initial particle motion exhibits no correlation to ejections (Q2) but would take place only when sweeps (Q4) reach the particle, which corresponds to the incoming hairpin head. *Detert et al.* [2010] simultaneously measured the near-bed velocity and pressure fields using the 2-D PIV and an array of pressure sensors. Based on the conditionally sampled velocity fields associated with the pressure-drop events, a bed destabilizing flow-pressure pattern was identified whereby the high-speed fluid of a hairpin packet reached the proximity of the bed in the sense of sweeps (Q4), resulting in a pressure drop and initial particle uplift, which in turn increased the exposed area of a target particle and the probability of entrainment.

[8] The above studies, all based on accurate PIV mapping of the 2-D velocity (u', v') fields, reveal a common result consistent with the conventional notion that sweeps (Q4) are most responsible for particle entrainment. It is, however, still unclear why the ejections (Q2) could effectively initiate particle uplift with their negative values of u'. Furthermore, it remains unresolved how those large-scale sweeps (Q4) could reach a bed particle and eventually lift up the particle if they are part of the hairpin head located above the shear layer, rolling over a low-speed zone and counteracted by the ejected fluid. A particle is dislodged from the bed when the force or moment balance is disrupted [*Wu and Chou*, 2003; *Valyrakis et al.*, 2010], the former corresponds to a lifting mode of entrainment while the latter corresponds to a rolling mode of entrainment. For an exposed particle (Figure 2a), the most probable mode of entrainment is rolling since the threshold of rolling is lower than that of lifting [*Wu and Chou*, 2003]. For a sheltered particle surrounded by the neighboring particles (Figure 2b), however, a lifting mode (or partial uplift) followed by rolling is the most probable mode of entrainment. In any case, the instantaneous drag or lift induced by the coherent motions should: (1) exceed the drag or lift associated with the background turbulence, and (2) apply directly on the particle. The ejections (Q2) or sweeps (Q4) reported in the above mentioned studies do not fully meet such criteria. Thus, a working model for the interactions between coherent structures and sediment entrainment remains a missing piece to be found.

2. Retrograde Spanwise Vortices

[9] Lately an experimental study [*Dwivedi et al.*, 2011] shed new light on the interactions between the coherent structure and particle entrainment, in which the PIV mapping of the 2-D velocity (u', v') field during particle entrainment reveals the presence of both prograde and retrograde vortices (i.e., spanwise vortices rotating, respectively, in the same sense as the mean shear and counter to the mean shear). They noted that the 2-D velocity (u', v') field was dominated for most of the time by prograde vortices. Such vortices, however, played no roles in particle entrainment. On the contrary, a convecting retrograde vortex, although rare and intermittent, was typically observed at the time of particle entrainment.

[10] The idea that sediment particles are entrained by retrograde vortices is, in fact, not new. In his pioneering work, *Sutherland* [1967] proposed a mechanism where entrainment of the sediment particles is due to what he called 'an incoming eddy from upstream'. This eddy rotates in such a way that the flow along its lowermost portion is in the direction of the mean flow. As this eddy disrupts the viscous sublayer and impinges on a particle it exerts a drag force in the direction of the local velocity, which as a result of the rotation within the eddy is inclined at a small angle to the bed in the sense of Q1 (outward interactions), as depicted in Figure 2a. Although *Sutherland* [1967] was then unable to prove the presence of such vortices, the idea that coherent structures contribute to particle entrainment has since inspired many generations of researchers, and after four decades such retrograde vortices finally came in our sight thanks to the advances in the PIV.

[11] The retrograde spanwise vortices revealed by the 2-D velocity (u', v') field may not be well known to the fluvial research community, but they have been extensively investigated over the last several years [*Christensen and Wu*, 2005; *Wu and Christensen*, 2006; *Natrajan et al.*, 2007], where the prograde vortices are characterized by negative spanwise vorticities ($\omega_z < 0$) while the retrograde vorticities are characterized by positive spanwise vorticities ($\omega_z > 0$). Their experimental studies, based on the high-resolution PIV mapping of the 2-D velocity (u', v') fields in turbulent channel flows over smooth beds, have shown that the very-near-bed region ($y < 0.1\ h$, h = flow depth) is densely populated with prograde vortices and most of them have structural signatures consistent with hairpin heads, which supports the previous finding that hairpin vortices are generated very close to the bed and grow into the outer layer as they convect downstream. In contrast, retrograde vortices are scarce in the very-near-bed region but most prominent at the outer edge of the log layer ($y \approx 0.2\ h$), often pairing with prograde vortices, consistent with the observations made in rough-bed channel flows [*Dwivedi et al.*, 2011]. Most retrograde vortices have diameters in the range between $25\ y_* \sim 55\ y_*$ with an upper bound of $\sim 100\ y_*$ [*Christensen and Wu*, 2005], where y_* ($=\nu/u_*$) is viscous length scale. For typical channel flows with kinematic viscosity of water $\nu = 10^{-6}$ m^2/s and shear velocity u_* in the order of 10^{-2} m/s, the sizes of the retrograde vortices would be <10 mm, comparable to the grain sizes of gravels and fine pebbles, which also resemble the vortex sizes shown by *Dwivedi et al.* [2011]. Based on a thorough analysis, *Natrajan et al.* [2007] interpreted that some of these retrograde-prograde pairing patterns are the spatial signatures revealed when an Ω-shaped hairpin is sliced through its shoulder by a streamwise-vertical measurement plane (Figure 1).

[12] Moreover, it could be implied by the field observations of *Smart* [2006] and *Smart and Habersack* [2007] that a passing retrograde vortex may also contribute to the

entrainment of fully sheltered particles. These researchers used a high-frequency differential pressure sensor installed in the gravels to detect the convecting pressure difference between the bed surface and subsurface (7 cm beneath bed surface), with the motion of the tracking-sensor stones being monitored simultaneously. Their results revealed that the convecting vertical pressure difference reached a level sufficient to lift the surface particle at the time the initial motion of a sensor stone was detected. An implication of the results is that entrainment of a fully sheltered particle can result from the net upward pressure (lift force) possibly induced by a convecting retrograde vortex without a need of the frontal-area-based hydrodynamic forces that are experienced by an exposed particle (Figure 2b). This is analogous to the bed-destabilizing pressure structure proposed by *Detert et al.* [2010], except that the Bernoulli pressure drop is not necessarily associated with sweeps (Q4) but may be induced by a retrograde vortex.

[13] With much being said about the presence of a retrograde vortex at the time of particle entrainment, however, direct measurements showing that the target particle is impinged by the lower portion of a retrograde vortex in the process of entrainment is still lacking. We argue that if entrainment of an exposed particle is associated with a passing retrograde vortex, as shown in Figure 2a, then the target particle should have experienced a majority of vortex-induced outward interactions (Q1) followed by sweeps (Q4). To test this hypothesis, we carry out a series of experiments to make near-particle measurements of the local 2-D velocities associated with particle entrainment events that are observed synchronously with the high-speed videography. Using a shifted-time cumulative quadrant fraction approach, we establish in a more direct manner the quadrant signature of a passing retrograde vortex. We also explore the difference in the quadrant signatures that would be detected at different locations during the passage of a retrograde vortex. Two types of pocket geometry are examined here, based on which we point out the potential discrepancy in the observed quadrant signatures that may arise when the velocity measurement plane is misaligned with the direction of particle entrainment.

3. Experiments

3.1. Experimental Setup

[14] The experiments were conducted in a 2.2-m-long, 20-cm-wide flume; at the inlet was a honeycomb flow regulator. The slope of the flume was adjusted to ensure a quasi-uniform free-surface flow in the 40 cm testing reach. The bottom of the flume was packed closely (hexagonally) with 8 mm spheres forming a flat, rough bed surface. A single target sphere, also 8 mm in diameter, was placed on the bed at a location 1 m downstream of the inlet, along the centerline. Observations of flow velocities and particle entrainment were made through the sidewall.

[15] A combination of LDV (Dantec Flowlite) and high-speed camera (Mikrotron MC1303) was used to measure flow velocities and record the images of particle entrainment events. The 2-D LDV comprised a 30 mW Nd:YAG green laser and a 10 mW HeNe red laser, which were used for measurements of streamwise and vertical velocity components, respectively. The laser beams, separated by 4 cm spacing, were focused through a lens of 40 cm focal length, forming an ellipsoidal measurement volume 0.1 mm in the vertical and streamwise extent and 2.4 mm in spanwise extent. The measurement volume was formed at a centerline spot 1 mm upstream from the edge and 1 mm below the top of the target sphere (Figure 3). This is the closest possible spot to the target particle due to the limitations of focal length and flume width (hereinafter referred to as near-particle spot). The water flow was seeded with 5 μm polyamide particles, which allowed for the mean data rates to exceed 200 Hz (measurements per second) and data validation ratios to be >95%. The high-speed camera was set to 200 fps (frames per second) and a resolution of 1,208 $\times$ 1,024 pixels. The LDV and high-speed camera were synchronized with an input signal so that the velocity data and images of particle entrainment can be analyzed later in a common time frame.

3.2. Experimental Procedure

[16] Before each run, we confirmed that a fully developed turbulent flow was established by examining the vertical profiles of mean streamwise velocity $\bar{u}$, root-mean-square (RMS) turbulence intensities σ_u and σ_v, and Reynolds stress $-\overline{u'v'}$ at three designated sections (at the centerline), i.e., at $x = 0$ (where the near-particle spot was located) and $x = \pm 2\ h$ (see section 3.4 for details). We then placed the target particle on the bed and waited for $\sim$30 s to ensure that the particle was held in place and not subjected to initial instabilities. The LDV and camera were then triggered synchronously; the velocity measurements and image recordings were continued until the target particle was fully entrained and dislodged. We did not count those events in which the target particle was partially entrained but such initial movement did not result in full entrainment. After being fully dislodged, the target particle was placed back to the original pocket. The same procedure was repeated, which allowed for >200 full entrainment events observed in a single set of experiments (Table 1).

[17] Identifying the initial time of particle motion was a crucial task in this study, which relied on the recorded images, as shown in Figure 4a, where the original edge of the target sphere is marked by a vertical line. While it is not uncommon to see the target particle vibrating, full entrainment of the particle would be typically characterized by a continuous, complete passage of the target particle over its edge line. Careful reviews of the motion pictures and converted images allowed us to identify the initial time of particle entrainment, which was set as the origin (τ = 0) of the shifted time frame in subsequent time series analyses, as shown in Figures 4b and 4c, where negative and positive values of τ denote the pre- and post-entrainment time, respectively.

3.3. Experimental Conditions

[18] Three sets of experiments (Sets 1$\sim$3) were performed (Table 1). Sets 1 and 2 involved entrainment of a target grain from the first type of pocket geometry (referred to as pocket 1), as shown in Figure 3a, while Set 3 involved entrainment of a target particle from the second type of pocket geometry (referred to as pocket 2), as depicted in Figure 3b. The major difference between pockets 1 and 2 was the direction of the downstream valley from which the entrained particle would

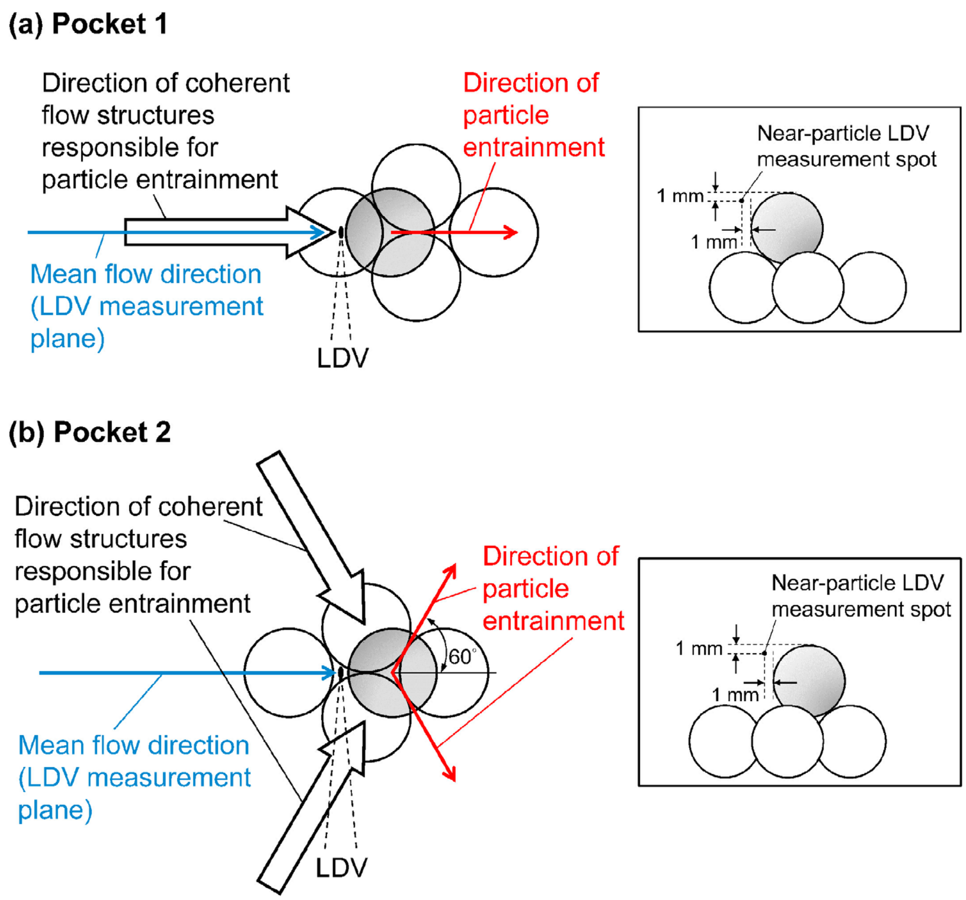

Figure 3. (a) Target particle set in pocket 1 (top view). The downstream valley of pocket 1 is in the same direction as the mean flow so that the direction of particle entrainment aligns with the LDV measurement plane. (b) Target particle set in pocket 2 (top view). The two diagonal valleys downstream of pocket 2 are at 60° with the mean flow direction so that the LDV measurement plane is misaligned with the direction of particle entrainment. (insets) Near-particle LDV measurement spot located 1 mm upstream and 1 mm below the target particle (side view along the centerline). LDV measurement volume not to scale.

Table 1. Experimental Conditions, Flow and Entrainment Characteristics, and Pre- and Post-entrainment Near-particle Velocity Statistics

Dataset	Total Number of Full Entrainment Events (Runs)	Initial Position (Specific Gravity) of Target Particle	h/D[a]	$\bar{U}$[b] (m/s)	Fr[c]	Re[d]	u_*[e] (cm/s)	k_s^+[f]	θ/θ_c[g]	Mean Frequency of Entrainment (1/s)	Pre-entrainment $\bar{u}_p$[h] (m/s) / $\sigma_{u,p}$[i] (m/s)	Pre-entrainment $\bar{v}_p$[h] (m/s) / $\sigma_{v,p}$[i] (m/s)	Post-entrainment $\bar{u}_p$ (m/s) / $\sigma_{u,p}$ (m/s)	Post-entrainment $\bar{v}_p$ (m/s) / $\sigma_{v,p}$ (m/s)
1	210	Pocket 1 (1.43)	6.1	0.140	0.20	6,900	1.63	130	0.26	0.011 (1/90)	0.091	0.019	0.108	0.001
											0.019	0.013	0.017	0.011
2	115	Pocket 1 (2.50)	8.6	0.390	0.47	26,900	4.01	320	0.46	0.029 (1/35)	0.196	0.050	0.238	0.001
											0.040	0.028	0.043	0.029
3	210	Pocket 2 (1.43)	8.0	0.187	0.24	12,000	1.73	140	0.30	0.016 (1/63)	0.129	0.037	0.165	0.001
											0.023	0.015	0.026	0.017

[a] h = flow depth, D = diameter of roughness elements = 8 mm.
[b] $\bar{U}$ = depth-averaged time-mean streamwise velocity.
[c] $\mathrm{Fr} = \bar{U}/\sqrt{gh}$ is Froude number, g = gravitational acceleration.
[d] $\mathrm{Re} = \bar{U}h/\nu$ is Reynolds number, ν = kinematic viscosity of water.
[e] u_* = bed shear velocity = $\sqrt{\tau_b/\rho}$, τ_b = bed shear stress, ρ = density of water.
[f] $k_s^+ = u_* k_s/\nu$ is roughness Reynolds number, k_s = roughness height = D.
[g] θ = Shields stress = $\tau_b/\rho g(s-1)D_p$, s = specific gravity of target particle, D_p = diameter of target particle = 8 mm, θ_c = critical Shields stress.
[h] $\bar{u}_p$ and $\bar{v}_p$ = near-particle streamwise and vertical mean velocities.
[i] $\sigma_{u,p}$ and $\sigma_{v,p}$ = near-particle root-mean-square (RMS) of streamwise and vertical velocity fluctuations u'_p and v'_p.

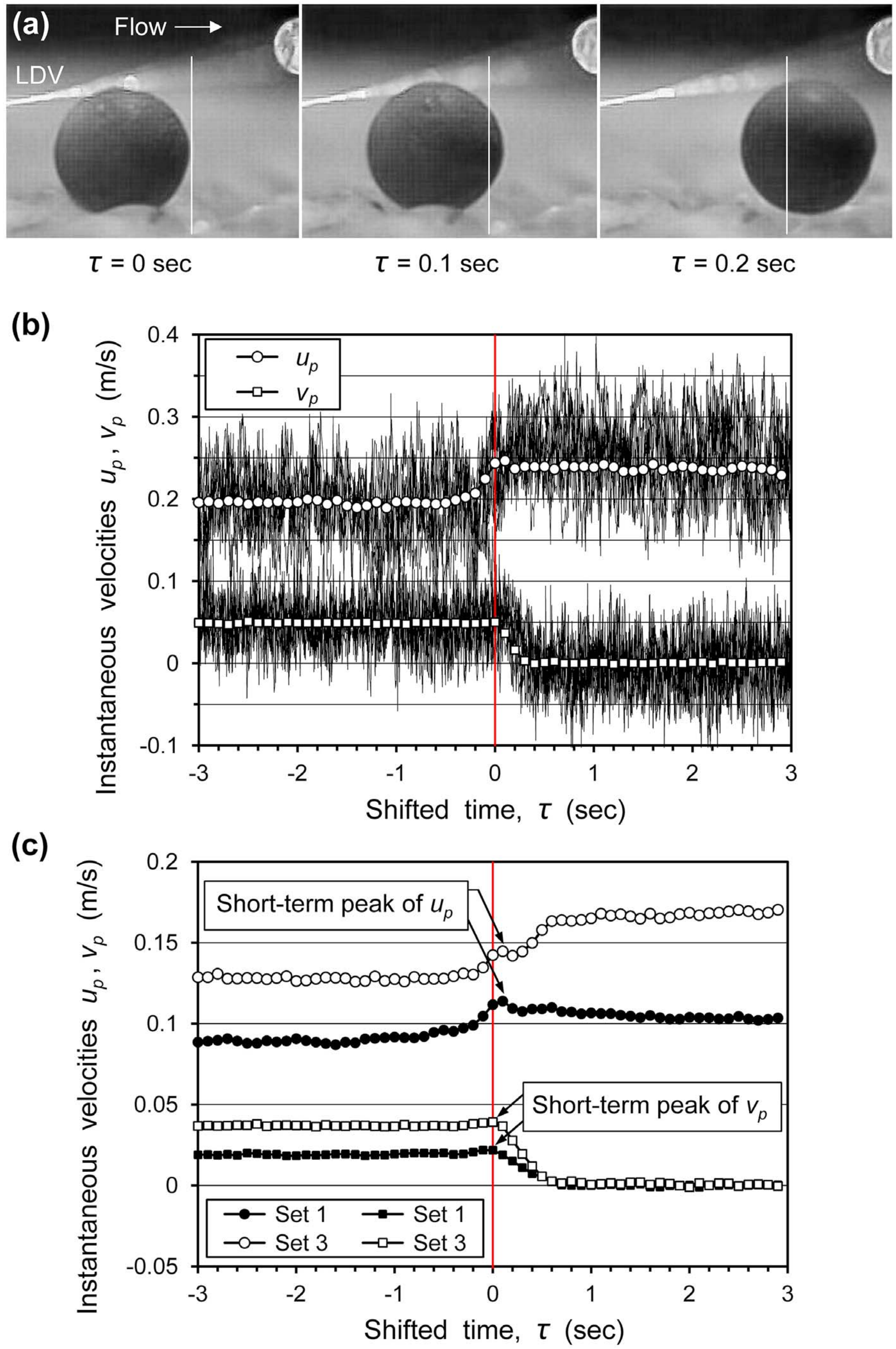

Figure 4. (a) Continuous images showing the initial motion ($\tau = 0$) and full entrainment of the target particle. Time series of near-particle velocities u_p and v_p measured from (b) Set 2 (five replicates overlapped), and (c) Sets 1 and 3. Open circles and squares denote the values of u_p and v_p averaged over 0.1-s intervals. The differences between pre- and post-entrainment u_p and v_p, and the short-term peaks of u_p and v_p present at $\tau \approx 0$ are demonstrated.

roll over. Pocket 1 was formed by three spheres relatively positioned in a way that the two cross-stream spheres were downstream of the third. The orientation of the valley immediately downstream of pocket 1 was in the same direction as the mean flow such that the direction of particle entrainment would align with the LDV measurement plane. In contrast, pocket 2 was formed by three spheres relatively positioned in a way that the two cross-stream spheres were upstream of the third. The two diagonal valleys immediately downstream of pocket 2 were at 60° with the mean flow direction such that the LDV measurement plane was misaligned with the direction of particle entrainment. As such, for Sets 1 and 2 the observed 2-D velocities may reflect the streamwise-vertical (x-y) signature of a flow structure that marches in the streamwise direction;

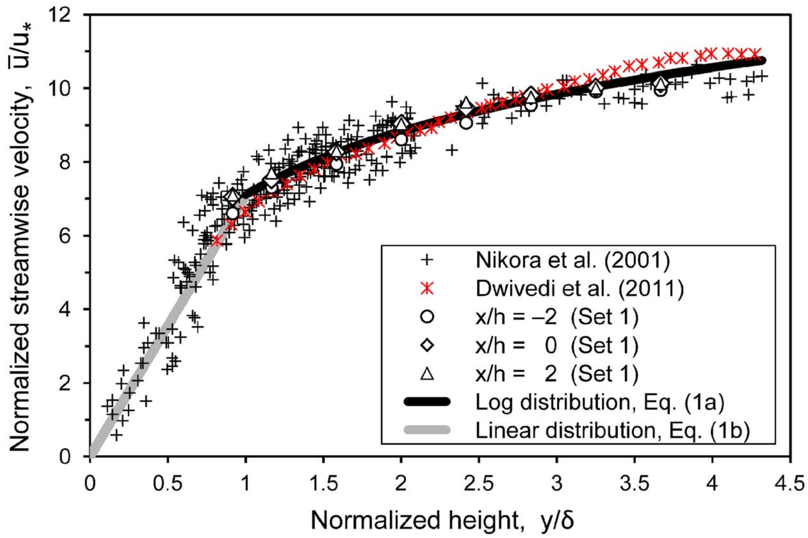

Figure 5. Profiles of normalized velocity $\bar{u}/u_*$ versus normalized height y/δ measured from Set 1 at three designated sections ($x = 0$ and $\pm 2\ h$). The profiles collapse on the logarithmic and linear velocity distributions suggested by *Nikora et al.* [2001] for fully developed turbulent open-channel flows over rough beds. Two published velocity measurements [*Nikora et al.*, 2001; *Dwivedi et al.*, 2011] are also shown for comparison.

while for Set 3 one may look at the streamwise-vertical signature of a structure that marches in oblique and thus is responsible for particle entrainment in the diagonal directions (see section 4.3).

[19] Experimental conditions are listed in Table 1. The flow was smallest in Set 1, with the relative submergence (=ratio of flow depth to diameter of roughness elements) $h/D = 6.1$ and depth-averaged mean streamwise velocity $\bar{U} = 0.140$ m/s; the flow was largest in Set 2, with $h/D = 8.6$ and $\bar{U} = 0.390$ m/s. The values of h/D reported here are typical of the depth-limited flows in gravel bed rivers [*Hardy et al.*, 2009]. Flows were all subcritical, with Froude numbers Fr ($=\bar{U}/\sqrt{gh}$, g = gravitational acceleration) constantly <0.5 and Reynolds numbers Re ($=\bar{U}h/\nu$) ranging from 6,900 to 26,900. Bed shear velocities u_* ($=\sqrt{\tau_b/\rho}$, τ_b = bed shear stress, ρ = density of water) were evaluated from the logarithmic fits to the velocity profiles (for details see section 3.4). Roughness Reynolds numbers k_s^+ ($=u_* k_s/v$) were all >70, indicating hydraulically rough flows, where k_s = roughness height, taken to be D for the rough beds [*Nikora et al.*, 2001]. Flow regimes were below threshold conditions, with the ratios of Shields stress to critical Shields stress, θ/θ_c, ranging from 0.26 to 0.46, comparable to the values (0.13∼0.4) reported by *Nelson et al.* [2001], where $\theta = \tau_b/\rho g(s - 1)D_p$, s = specific gravity of target particle, D_p = diameter of target particle, and the critical Shields stress θ_c (=0.03) was estimated with the modified Brownlie relation [*Parker*, 2008]. Rolling was observed to be the unique mode of entrainment, with the mean frequency of entrainment ranging from $(90\ \text{s})^{-1}$ to $(35\ \text{s})^{-1}$.

3.4. Mean Velocity, Turbulence Intensity, and Reynolds Stress

[20] Before we proceed, it is essential to examine whether a fully developed turbulent flow was established. Shown in Figure 5 are vertical profiles of the mean streamwise velocity $\bar{u}$ measured from Set 1 at three designated sections ($x = 0$ and $\pm 2\ h$). The measured profiles of $\bar{u}$ collapse on the logarithmic and linear velocity distributions suggested by *Nikora et al.* [2001] for the fully developed turbulent open-channel flows over rough beds, which take the following forms:

$$\frac{\bar{u}}{u_*} = \frac{1}{k}\ln\left(\frac{y}{\delta}\right) + C \quad \text{for} \quad \delta < y < 0.2h \tag{1a}$$

$$\frac{\bar{u}}{u_*} = C\left(\frac{y}{\delta}\right) \quad \text{for} \quad y \le \delta, \tag{1b}$$

where k = von Kármán constant (=0.4); y = distance above the bed; δ = thickness of the linear (or roughness) layer, which varies with the size and geometry of roughness elements, typically ranging between $D/2 \sim 2D$; C = velocity coefficient, a value of 7.1 is adopted following *Nikora et al.* [2001]. Equations (1a) and (1b) are, respectively, used to describe the velocity profiles in the logarithmic and linear layers, valid only when $h \gg D$. For the outer layer ($y > 0.2\ h$), the velocity distribution may be described by the velocity defect law [*Nezu and Nakagawa*, 1993]. Figure 5 shows that most of our measurements were made in the logarithmic layer; only the lowermost ones were measured at the margin of the linear layer. For comparison, two published sets of velocity data measured in the fully developed rough-bed open-channel flows [*Nikora et al.*, 2001; *Dwivedi et al.*, 2011] are also shown in Figure 5, where the data of *Nikora et al.* [2001] were measured at a wider range of depth covering both the logarithmic and linear layers, while the data of *Dwivedi et al.* [2011], like ours, were mostly measured in the logarithmic layer. The values of (δ, h) for our data, and the data of *Nikora et al.* [2001] and *Dwivedi et al.* [2011] are (1.2 cm, 4.9 cm), (2.1 cm, 13.5 cm) and (2.8 cm, 10.8 cm),

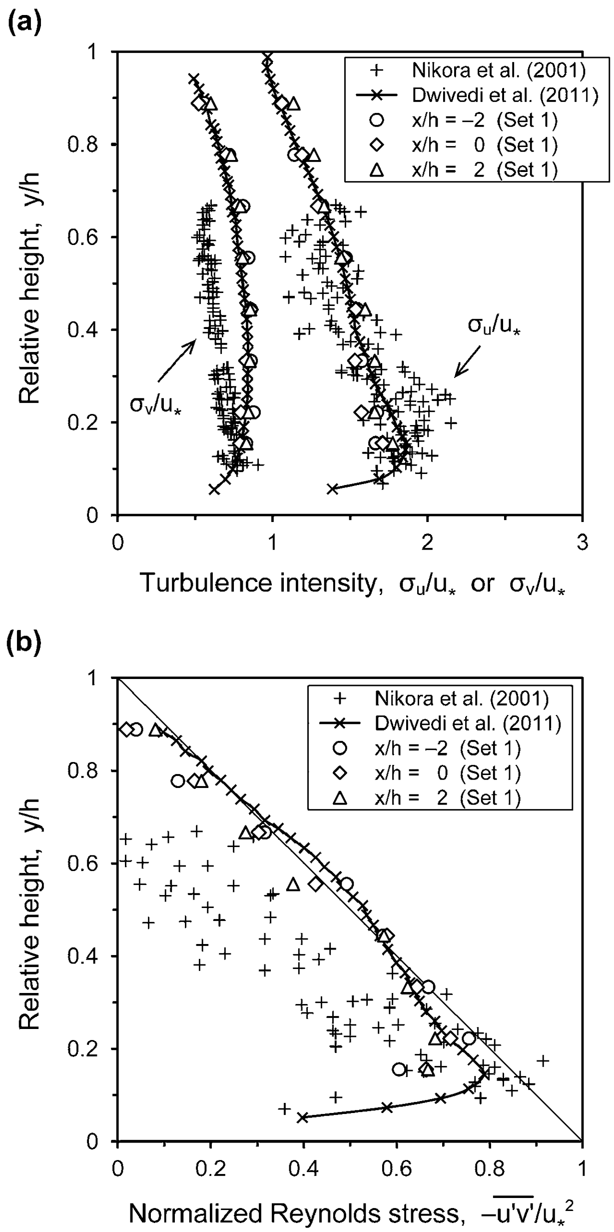

Figure 6. Vertical profiles of normalized (a) RMS turbulence intensities σ_u/u_* and σ_v/u_*, and (b) Reynolds stress $-\overline{u'v'}/u_*^2$ measured from Set 1 at three designated sections (x = 0 and ± 2 h). The straight line in Figure 6b indicates the linear distribution of Reynolds stress in the far-bed region. Two published data from fully developed rough-bed channel flows [*Nikora et al.*, 2001; *Dwivedi et al.*, 2011] are also shown for comparison.

respectively. The resemblance between our result and those measured in the fully developed rough-bed turbulent channel flows is clearly shown in Figure 5. Such profiles agree with those observed in natural gravel bed rivers [*Nikora and Smart*, 1997; *Roy et al.*, 2004]. Similar results were also obtained for Sets 2 and 3.

[21] Shown in Figure 6a are vertical profiles of the RMS turbulence intensities σ_u and σ_v measured from Set 1 at three designated sections x = 0 and ± 2 h, along with two published distributions of turbulence intensities in fully developed rough-bed channel flows [*Nikora et al.*, 2001; *Dwivedi et al.*, 2011]. The measured profiles of σ_u/u_* and σ_v/u_* appear to follow closely the published profiles, in particular those of *Dwivedi et al.* [2011], where the turbulence intensities σ_u and σ_v reach maxima at $y/h \approx 0.1$ and 0.2, respectively, below which σ_u and σ_v decrease toward the bed due to the effect of boundary roughness. Such decline of σ_v was to some extent captured by our measurements, however, the decline of σ_u was not observed due to the instrumental limitations.

[22] Shown in Figure 6b are vertical profiles of the normalized Reynolds stress $-\overline{u'v'}/u_*^2$ corresponding to the data presented in Figures 5 and 6a. Similarly, our profiles of $-\overline{u'v'}/u_*^2$ are consistent with the published distributions, especially with that of *Dwivedi et al.* [2011]. The vertical distributions of Reynolds stress are linear in the far-bed region, but decline toward the bed as the viscous stress and form-induced stress become significant in the near-bed region due to the influence of boundary roughness. Such decline of the Reynolds stress near the bed was captured by our lowermost measurements. In summary, comparison of our observed profiles of mean velocity, turbulence intensities, and Reynolds stress with the published measurements made in fully developed turbulent open-channel flows over rough beds may serve as an indication of the data quality and established flow conditions.

3.5. Near-Particle Velocity Measurements

[23] In this study the local flow velocities were measured at a spot in close proximity to the target particle (Figure 3). Due to the presence of the target particle in front of this spot, a rapid change in local velocities was detected at this spot during particle entrainment. Shown in Figure 4b are time series of the near-particle velocities u_p and v_p (here subscript p specifically indicates that the velocities were measured at the near-particle spot), where five replicates from Set 2 are overlapped to illustrate the collective pattern, and the open circles and squares denote the values of u_p and v_p averaged over 0.1-s intervals (using data from 115 runs). The differences between the pre- and post-entrainment velocities are clearly seen. Prior to particle entrainment, the near-particle mean velocities $\bar{u}_p$ and $\bar{v}_p$ were ~0.2 m/s and 0.05 m/s (Table 1) due to the streamline deflection in the presence of the target particle. After the target particle was fully dislodged and the obstruction to the flow was removed, $\bar{u}_p$ increased to ~0.24 m/s while $\bar{v}_p$ ceased to be zero. Similar changes in $\bar{u}_p$ and $\bar{v}_p$ during particle entrainment were also observed in Sets 1 and 3, as shown in Figure 4c and Table 1. The 0.1-s averaged values of u_p further exhibited a rapid rise prior to particle entrainment (τ = 0) and a short-term peak immediately afterwards. Such short-term peak of u_p was also observed in Sets 1 and 3, as shown in Figure 4c.

[24] It should be noted here that the local velocities measured at a spot close to the target particle facilitate the possibility of detecting nearly the real-time velocities impinging on the target particle, rendering the time lag and spatial variation between the measurement spot and upstream face of the target particle almost negligible. This approach is different from that used by previous investigators [e.g., *Schmeeckle et al.*, 2007; *Diplas et al.*, 2008; *Dwivedi et al.*,

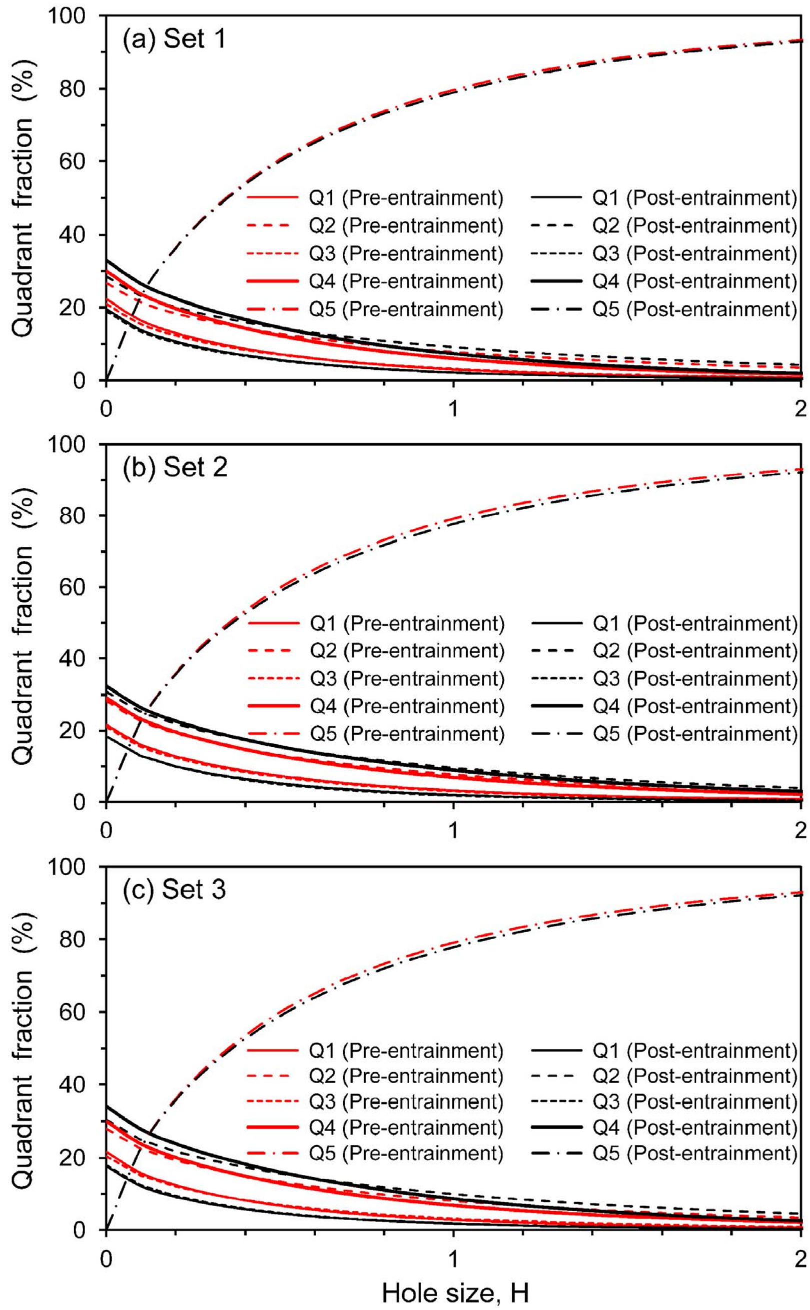

Figure 7. Pre- and post-entrainment long-term quadrant structures of (a) Set 1, (b) Set 2, and (c) Set 3 versus hole size H. The quadrant fractions Q_i (i = 1, 2, 3, 4, 5) are evaluated with the threshold quadrant detection technique (see text for details).

2011], in which the approaching flow velocities were measured at a spot located $1D$ upstream of the target particle with an acknowledgment that the local velocities at the spot are sufficiently close to the particle but not significantly affected by the presence of the particle. Their velocity measurements were then used to evaluate the instantaneous hydrodynamic forces acting on the target grain while Taylor's frozen turbulence hypothesis was used to accommodate the lag between velocity measurement and particle entrainment. In this study we adopted a near-particle approach to detecting local velocity fluctuations because the quadrant signature of a passing coherent structure is of our primary interest, and we see this as an alternative approach and potentially a new contribution to the area of research. However, a concern that may arise is the influence of the target particle on the turbulence characteristics observed at this near-particle spot. To clarify this, we examine below the long-term quadrant structures and power spectra of local velocities observed at the near-particle spot in the presence of the target particle (at pre-entrainment stage) and in the absence of the target particle (at post-entrainment stage).

[25] Shown in Figure 7 are the pre- and post-entrainment long-term quadrant structures of Sets 1~3 varying with the hole size H, where the quadrant fractions Q_i (i = 1, 2, 3, 4, 5)

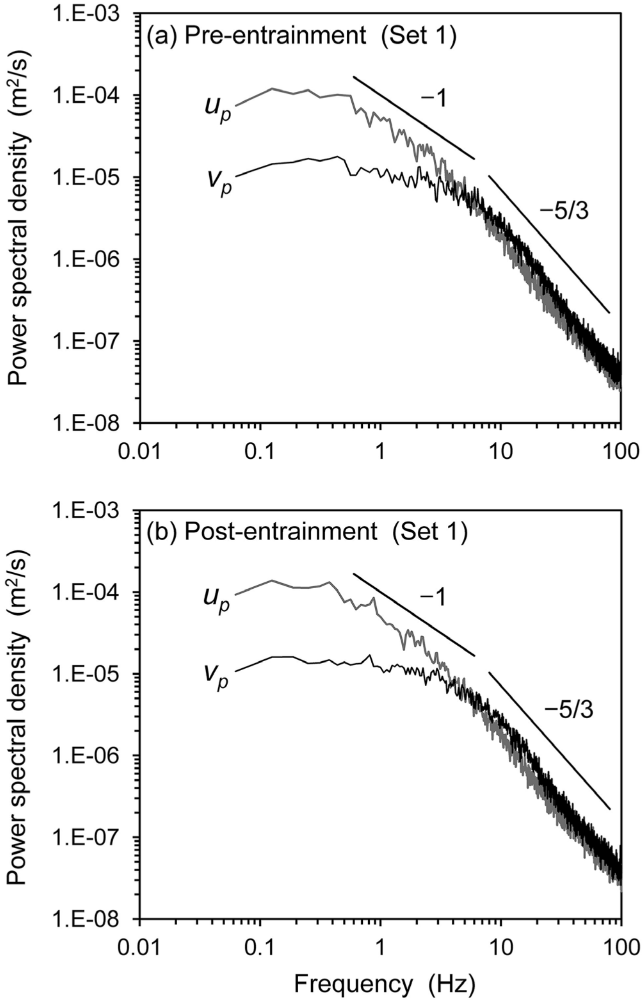

Figure 8. (a) Pre-entrainment and (b) post-entrainment power spectra of near-particle velocities u_p and v_p measured from Set 1. The pre- and post-entrainment near-particle velocity spectra exhibit similar scaling with the frequency. At frequencies >10 Hz, an inertial subrange follows the $-5/3$ power law; at frequencies <10 Hz, a production subrange scales with the -1 spectral slope.

are evaluated using the threshold quadrant detection technique [*Lu and Willmarth*, 1973]:

$$\gamma = \frac{|u_p' v_p'|}{\sigma_{u,p}\sigma_{v,p}} \geq H \quad \text{for} \quad Q_i, i = 1, 2, 3, 4 \tag{2a}$$

$$\gamma = \frac{|u_p' v_p'|}{\sigma_{u,p}\sigma_{v,p}} < H \quad \text{for} \quad Q_i, i = 5, \tag{2b}$$

where u_p' ($=u_p - \bar{u}_p$) and v_p' $(= v_p - \bar{v}_p)$ are near-particle streamwise and vertical velocity fluctuations; $\sigma_{u,p}$ and $\sigma_{v,p}$ = RMS intensities of u_p' and v_p' (see Table 1). Equation (2) is a conditional sampling where only stronger instantaneous Reynolds stresses with $\gamma \geq H$ are counted as the quadrant fractions Q_i (i = 1, 2, 3, 4) and all other weaker ones with $\gamma < H$ are counted as the fraction of 'hole events' (Q_i, i = 5). The results from Sets 1∼3 demonstrate consistently the trends that the quadrant fractions Q_i (i = 1, 2, 3, 4) decrease with H whereas the fraction of hole events Q_5 increases with H. As the hole size H increases from 0 to 2, the fractions Q_2 and Q_4 decrease from ∼30% to <5% and the fractions Q_1 and Q_3 decline from ∼20% to <1%, while Q_5 increases from 0 to >90%. The trends shown in Figure 7 are similar to those previously observed in the near-bed region of rough-bed channel flows [*Nakagawa and Nezu*, 1977; *Mignot et al.*, 2009]. The pre- and post-entrainment long-term quadrant structures, however, exhibit some minor differences that are consistent among the data sets for the examined range of hole sizes. Specifically, the pre-entrainment fractions Q_2 and Q_4 are consistently smaller than their post-entrainment counterparts, while the pre-entrainment fractions Q_1 and Q_3 are consistently greater than their post-entrainment counterparts, and the pre-entrainment Q_5 slightly exceeds its post-entrainment counterpart. The differences between the pre- and post-entrainment long-term quadrant structures suggest that the local turbulence characteristics were influenced by the presence of the target particle, with the long-term fractions of Q2 and Q4 reduced at most by 1.8∼4%, and the long-term fractions of Q1 and Q3 increased at most by 2∼4.1%, while the long-term fraction of hole events (Q5) increased by <1.5%. The effects of the target particle on the near-particle turbulence characteristics are, however, not necessarily problematic because, as we will demonstrate later in section 4, it is still those short-term (and probably slightly distorted) coherent structures that are associated with particle entrainment.

[26] Shown in Figure 8 are the pre- and post-entrainment power spectra of near-particle velocities u_p and v_p measured from Set 1. The pre- and post-entrainment velocity spectra exhibit very similar scaling with the frequency. At frequencies >10 Hz, an inertial subrange characterized by a roll-off that follows the Kolmogorov $-5/3$ power law is observed. At frequencies <10 Hz, a production subrange scaled with a -1 spectral slope is attributable to the turbulent events in which the energy production and cascade energy transfer coexist [e.g., *Nikora*, 1999; *Singh et al.*, 2010; *Dey et al.*, 2011]. In this subrange, the streamwise velocity spectrum contains more energy than its vertical counterpart, consistent with the results previously observed in rough-bed channel flows [*Voulgaris and Trowbridge*, 1998; *Shvidchenko and Pender*, 2001]. In the inertial subrange, however, the energy level of the vertical velocity spectrum is slightly higher than its streamwise counterpart, in agreement with the relative ratio (=4/3) predicted by the Kolmogorov spectra model [*Pope*, 2000] and the result previously obtained in gravel bed channel flows [*Shvidchenko and Pender*, 2001]. No significant differences are found between the pre- and post-entrainment velocity spectra observed at the near-particle spot.

4. Results and Discussion

4.1. Quadrant Signatures Observed During Particle Entrainment

[27] The flowfield under investigation is a superposition of the background turbulence field and coherent motion field, the former is characterized by the long-term quadrant structure while the latter is reflected by the intermittent short-term quadrant signature. To observe the long-term

background quadrant structure with the LDV is relatively easy, whereas to detect the intermittent coherent motions using the point measurements can be extremely difficult. To facilitate a quantitative detection of the short-term (or quasi-instantaneous) quadrant signature at a time point of interest, we devise a 'shifted-time cumulative quadrant fraction approach' in which the cumulative quadrant fractions $F_i(\tau - \tau_0)$ are evaluated with respect to a time point τ_0 in the shifted time frame, as defined by

$$F_i(\tau - \tau_0) = \frac{N_i(\tau - \tau_0)}{\sum_{j=1}^{4} N_j(\tau - \tau_0)} \quad \text{for} \quad i = 1, 2, 3, 4 \qquad (3)$$

where $\tau = t - t_E$ = shifted-time variable, here t = arbitrary time, t_E = initial time at which a full entrainment event starts; τ_0 = time point of interest; $N_i(\tau - \tau_0)$ = number of ith-quadrant events in the time period $(\tau - \tau_0)$. If $\tau_0 = 0$ is taken, the quadrant fractions $F_i(\tau - 0)$ will exhibit the pre- and post-entrainment cumulative structures, where negative and positive values of $\tau(=\tau - 0)$ represent pre- and post-entrainment time periods, respectively. There are two extreme conditions associated with this approach. First, as $\tau \to \mp\infty$, $F_i(\tau - 0)$ would exhibit the pre- or post-entrainment long-term quadrant fractions. Second, as $\tau \to 0$, the number of events $N_i(\tau - 0)$ in the time period τ would be too small to be statistically meaningful. To accommodate this, the shortest time period (τ = 0.03 s) adopted herein is to secure that at least 1,000 pairs of (u_p', v_p') are included in the calculations of $F_i(\tau - 0)$.

[28] The proposed shifted-time cumulative fraction approach, in a sense, resembles the velocity decomposition method used by *Hussain* [1983] and *Blanckaert and de Vriend* [2005], where the velocity fluctuations were decomposed into rapid and slow components, the former represents the background turbulence whereas the latter reflects the coherent motions. Their split of velocity fluctuation components was made by taking the moving average over a time period long enough to eliminate rapid fluctuations but short enough not to lose essential information on slow fluctuations. Our approach needs no criterion for splitting quadrant structures associated with background turbulence and coherent motions, instead, transitions between the long- and short-term structures are exhibited through the variation of τ.

[29] Shown in Figure 9a are the pre- and post-entrainment cumulative quadrant fractions versus the shifted time τ, which were obtained based on an ensemble of all data from Set 1. A short-term spiky rise of the Q1 fraction up to >50% prior to the initial time of particle entrainment (τ = 0) is clearly demonstrated, despite that the pre-entrainment long-term fraction of Q1 only amounts to 22%. This pre-entrainment short-term rise of the Q1 fraction is followed by a drastic drop to ~30% immediately afterwards and a cumulative declining trend toward its long-term fraction in background turbulence. A pre-entrainment increasing trend is also observed for the Q4 fraction, which is, however, much milder than that of the Q1 fraction and is associated with a small drop prior to entrainment. After particle entrainment, the Q4 fraction becomes the dominant one (>40%), which is then followed by a cumulative declining trend toward its long-term fraction in background turbulence. By contrast, prior to particle entrainment the Q2 and Q3 fractions exhibit fast declines to ~10%, followed by post-entrainment cumulative increasing trends toward their long-term fractions. Note that the short data gap after τ = 0 is due to the continuous motion of the target particle during which no single $(\bar{u}_p, \bar{v}_p)$ can be used to extract (u_p', v_p').

[30] In view of Figure 9a, it is highly possible that particle entrainment is a result of the interactions with a passing retrograde vortex. As a retrograde vortex approaches the target particle, dominance of the Q1 fraction would be detected at the near-particle spot (Figure 2a). Along the way the Q4 fraction would continue to increase, which in turn would lead to the declines of the Q2 and Q3 fractions. The small drop in the Q4 fraction prior to particle entrainment does not mean that the number of the Q4 events is declined. Rather, it arises from the slower increase of the Q4 fraction compared to the increase of the Q1 fraction. After τ = 0 and the passage of the vortex, the dominance of the Q4 fraction would be detected, while the Q1 fraction would exhibit a rapid decline. It is when the vortex moves further downstream, the long-term quadrant structure of the background turbulence would resume.

[31] There is a possibility that the quadrant signature observed at the near-particle spot may result from the presence of the target particle. If the observed pre-entrainment dominance of Q1 and post-entrainment dominance of Q4 is merely a result of the particle-induced flow deflection, such pattern would remain as a constant quadrant signature at any selected time point of interest. To examine whether this is true, we provide in Figure 10 four examples showing the shifted-time cumulative quadrant fractions $F_i(\tau - \tau_0)$ obtained with different points of interest τ_0. The quadrant signatures shown in Figure 10 are rather different from that shown in Figure 9a. Specifically, any quadrant could emerge as the dominant one if the focus is placed at different τ_0. For example, Q1 is dominant at $\tau_0 = -26.9$ s, Q2 dominates at $\tau_0 = -26.0$ s, Q3 constitutes the largest fraction at $\tau_0 = -20.5$ s, and Q4 is the dominant one at $\tau_0 = -21.8$ s. In view of these results, it can be concluded that the quadrant signature seen in Figure 9a is not necessarily resulting from the presence of the target particle in front of the measurement spot, nor is it an invariable outcome of the proposed sampling approach. Rather, it is highly probable that the observed short-term quadrant signature is indicative of a passing retrograde-vortex-type coherent structure.

[32] To confirm the reproducibility of our result, an additional set of experiments (Set 2) including 115 runs of full entrainment were performed with a much greater flow (Table 1), with the value of Re about 4 times that used in Set 1. Shown in Figure 9b are the pre- and post-entrainment cumulative quadrant fractions obtained based on an ensemble of all data from Set 2. The variation patterns of the quadrant signature are consistent with those shown in Figure 9a, only now the transitions between the long- and short-term quadrant structures are faster than those seen in Figure 9a. A pre-entrainment spiky rise of the Q1 fraction from ~23% to ~45%, and a milder rise of the Q4 fraction from ~33% to ~42% followed by a small drop to ~36% prior to particle entrainment, accompanied by declines of the Q2 and Q3 fractions to <10%, are observed (Figure 9b). Note that the transitions between the long- and short-term

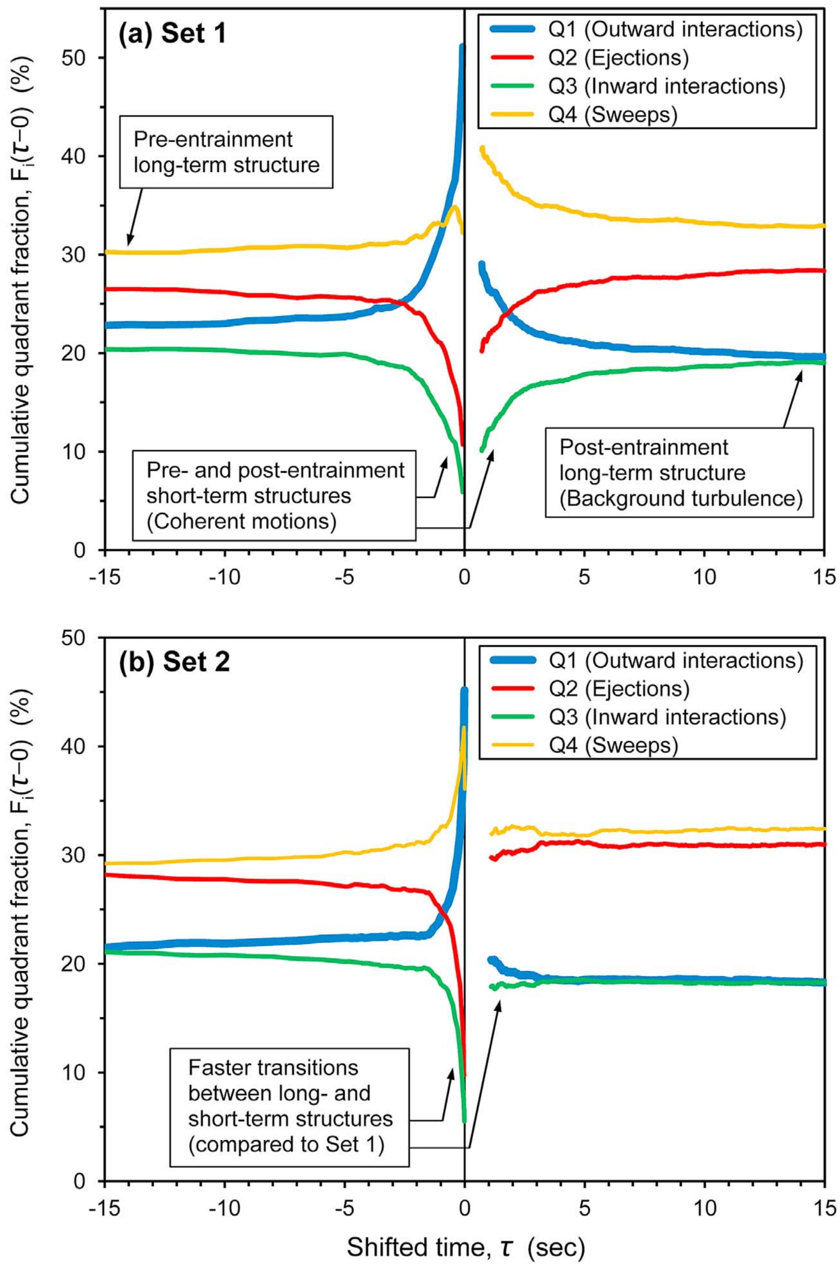

Figure 9. Pre- and post-entrainment cumulative quadrant fractions $F_i(\tau - 0)$ versus shifted time τ, based on a compilation of all data from (a) Set 1, and (b) Set 2. The data gap after $\tau = 0$ is due to the continuous movement of the target particle during which no single $(\bar{u}_p, \bar{v}_p)$ can be used to extract (u'_p, v'_p).

structures is much faster in Set 2 than that observed in Set 1. For example, the Q1 fraction is increased ~22% in ~2 s while the Q4 fraction is increased ~9% in the same time period but then declined ~6% in ~0.03 s immediately before $\tau = 0$, much faster than the corresponding drop of the Q4 fraction (~3% in ~0.3 s) observed in Set 1. After particle entrainment, the Q1 fraction drops drastically to <20% while the Q4 fraction becomes the dominant one remaining at ~32%, both exhibiting very mild cumulative declining trends toward their long-term background fractions, whereas the Q2 and Q3 fractions exhibit very mild cumulative rising trends toward their long-term background fractions.

[33] Our observations agree with the earlier result obtained by synchronous applications of the force transducer, LDV, and PIV mapping of the 2-D velocity field associated with a turbulence event in which the instantaneous hydrodynamic forces acting on the test particle were high enough to initiate particle motion [*Nelson et al.*, 2001]. This event had higher than average velocities over the particle (in the sense of Q1) and downward velocities at the upstream face of the particle (in the sense of Q4). Their experimental result suggested that these rare turbulence events are closely tied coherent structures on the same scale as the particle size, which produce net pressures favorable to particle entrainment in situations

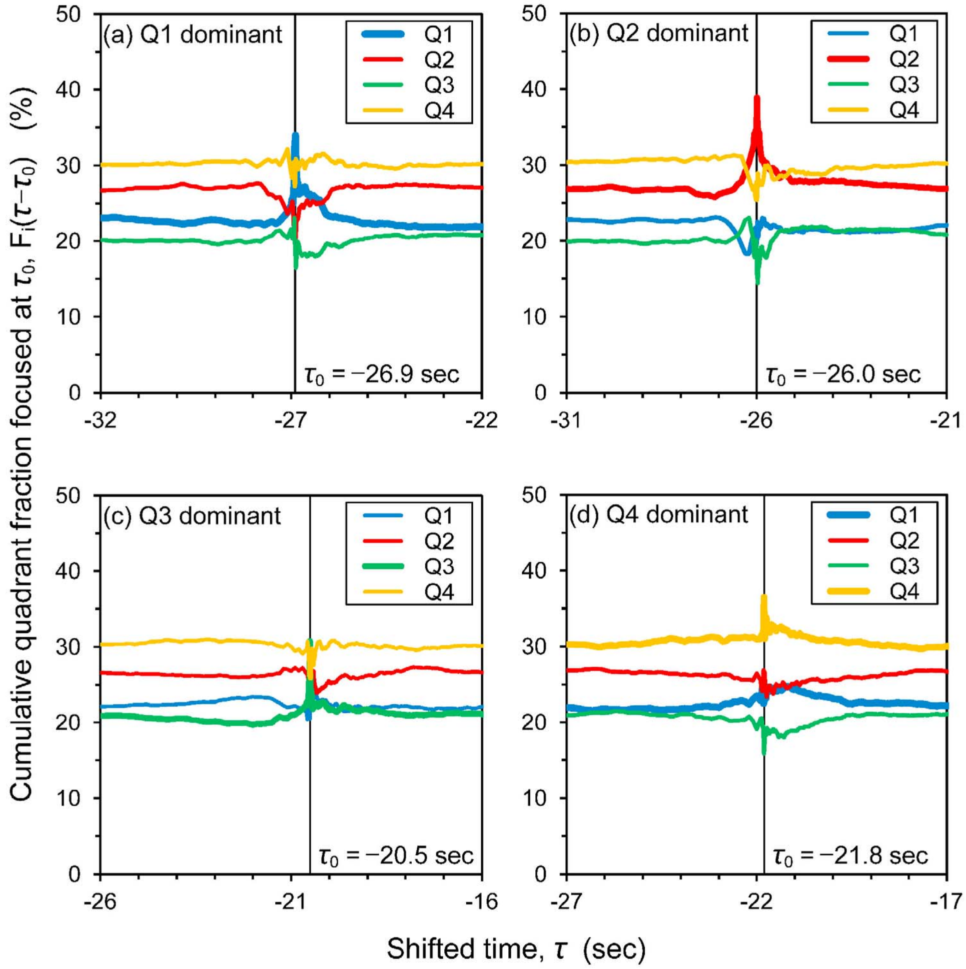

Figure 10. Four examples showing the shifted-time cumulative quadrant fractions $F_i\ (\tau - \tau_0)$ obtained with different points of interest τ_0. The results reveal that any quadrant can emerge as the dominant one when the focus is placed at different τ_0.

where average flow conditions would predict no particle motions.

4.2. Quadrant Signatures Observed at Different Locations

[34] In this section we use the theoretical solution of a simplified model flow to explore the difference in the quadrant signatures observed at different locations during the passage of a retrograde vortex, and compare the theoretical prediction with experimental data collected from different measurement spots. A retrograde vortex that passes a target particle in the coherent motion field can be modeled with a simplified 2-D potential flow in the z-plane, as depicted in Figure 11a, where the vortex is located at $z_0 = (x_0, y_0)$ and advancing with a self-induced speed V_s, r = radius of the target particle, whose center is set as the origin of the z-plane, and y_0 is taken to be 0.2 h for retrograde vortices [*Wu and Christensen*, 2006; *Dwivedi et al.*, 2011]. Note that V_s is a velocity that would be seen in the coherent motion field, the vortex convection speed V_c in the superimposed flowfield is $V_c = V_a + V_s$, where V_a = mean advection velocity of the background turbulent flow [*Doligalski et al.*, 1994].

[35] As illustrated in Figure 11, the z-plane (physical plane) can be mapped to the Z-plane (transformed plane) by means of the Joukowski transformation [*Pao*, 1967; *Milne-Thomson*, 1968], which is expressed as

$$Z = z + \frac{r^2}{z}, \tag{4}$$

where $z = x + iy$ and $Z = X + iY$ are complex variables. The semicircular solid boundary in the z-plane would map into a flat plate in the Z-plane, and the vortex center z_0 would map to $Z_0 = (X_0, Y_0)$, where $Y_0 = a$ corresponds to $y_0 = 0.2\ h$. An existing theoretical solution of the 2-D potential flow concerning a vortex pair advancing in the X-direction of the Z-plane (Figure 11b) can be applied to determine the corresponding velocity field in the z-plane, as described below in more detail.

[36] A retrograde vortex of strength κ located at a distance a above a flat plate will be convected to the right with a self-induced speed $\kappa/2a$ due to the presence of the plate, as if it is convected by the flowfield of its mirror image below the plate (Figure 11b). Since the retrograde vortex in the Z-plane is a transformation of the retrograde vortex in the z-plane,

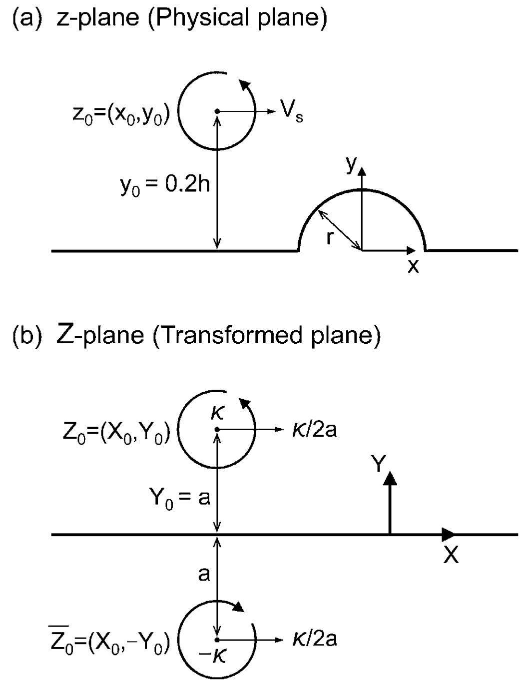

Figure 11. (a) A simplified 2-D potential flow in the z-plane (physical plane) used to model a retrograde vortex passing the target particle in the coherent motion field. The vortex is located at $z_0 = (x_0, y_0)$ and advancing with a self-induced speed V_s. (b) The z-plane is mapped to the Z-plane by means of the Joukowski transformation. The semicircular solid boundary in the z-plane maps into a flat plate in the Z-plane; the vortex center z_0 maps to $Z_0 = (X_0, Y_0)$. A retrograde vortex of strength κ located at a distance a above the plate is convected to the right with a self-induced speed $\kappa/2a$ due to the presence of the plate, as if it is convected by the flowfield of its own mirror image below the plate.

the single vortex above the solid boundary in the z-plane is equivalent to the single vortex above the plate in the Z-plane, which, due to the image-flow effect induced by the plate, is equivalent to a pair of vortices each of strength κ but of opposite rotations separated by a distance $2a$ bisected by the X-axis, where the vortex pair advances with a speed $\kappa/2a$. The complex potential w of the flowfield takes the following form [*Milne-Thomson*, 1968]:

$$w = i\kappa\left(\log \frac{Z - Z_0}{Z - \bar{Z}_0}\right), \tag{5}$$

where $\bar{Z}_0 = (X_0, -Y_0)$ is the complex conjugate of Z_0. The complex potential is typically defined by $w = \phi + i\psi$, (ϕ, ψ) = velocity potential and stream function of a 2-D potential flow. By virtue of the Cauchy-Riemann relations [*Pao*, 1967; *Milne-Thomson*, 1968], the velocity components (u', v') of the vortex-induced coherent motion field in the z-plane can be determined with the derivative of the complex potential:

$$\frac{dw}{dz} = \frac{dw}{dZ}\frac{dZ}{dz} = i\kappa\left(\frac{1}{Z - Z_0} - \frac{1}{Z - \bar{Z}_0}\right)\left(1 - \frac{r^2}{z^2}\right) = u' - iv'. \tag{6}$$

That is, the real part of (6) is the x-component velocity, and the imaginary part of (6) is the negative y-component velocity. To determine the velocity field in the z-plane, one needs to specify the position z_0 of the vortex center and the locations z at which the velocities are to be determined. Through (4), z and z_0 are transformed to Z and Z_0 (and $\bar{Z}_0$), which serve as the input to (6) for obtaining the output velocity components (u', v').

[37] The velocity field so obtained is shown in Figure 12, where the vortex is located at $(-2r, 0.2\,h)$ and velocities are presented in the nondimensionalized forms $(u'r/\kappa,\ v'r/\kappa)$. The vortex-induced coherent motion field is clearly shown in Figure 12, where the velocity vector detected at the near-particle spot A is different from that detected at spot B located $1D$ upstream of the target particle. The former is in the sense of Q1 while the latter is in the sense of Q4, which demonstrate the difference in the quadrant signatures that would be observed at different measurement spots. To further complicate this is the convective nature of the vortex, that is, the vortex would advance in the x-direction with a speed V_s. Shown in Figure 13 are the nondimensionalized velocity components observed at spots A and B as the vortex advances from the upstream to downstream of the target particle ($x_0 = -10\,r$ to $10\,r$). It is shown that, with the target grain remaining stationary, Q1 (outward interactions) is the vortex-induced quadrant signature that would be observed at spot A (Figure 13a), while at spot B, Q1 (outward interactions) is observed when the vortex is located upstream but then Q4 (sweeps) is detected as the vortex becomes located downstream of spot B (Figure 13b).

[38] The theoretical predictions are tested against the velocity measurements collected from spots A and B during particle entrainment. First, the result shown in Figure 13a is compared with our near-particle instantaneous velocities observed at spot A (Figures 4b and 4c). Note that the x-axis in Figure 13 can be viewed as equivalent to the time axis obtained with the locations x_0 divided by V_s. The three sets of instantaneous velocities shown in Figures 4b and 4c demonstrate a consistent pattern that exhibits the short-term peaks present at $\tau \approx 0$. The short-term peaks of u_p are more significant than those of v_p, and the peak of u_p typically takes place at a time immediately after $\tau = 0$, while the peak of v_p would occur at $\tau = 0$. Such differences in the magnitude and timing between the short-term peaks of u_p and v_p are in agreement with the theoretical prediction shown in Figure 13a, where the peak magnitude of u' is $\sim$ twice the peak magnitude of v', and the peak of u' lags behind the peak of v' by a small distance ($\approx r$). However, the predicted unique Q1 observed at spot A should not be interpreted as that only Q1 would be detected at this spot during the passage of a retrograde vortex. Given the fact that the observed flowfield is a superposition of the background turbulence field and vortex-induced coherent motion field, the quadrant structure observed at spot A would be affected by the passing vortex only when the vortex becomes close and strong enough to be sensed. Also, the results presented in Figure 13 are derived for the condition of a stationary target particle, after the particle is entrained (at $x_0/r \approx -2$ where v' peaks) the effect of the target particle on the near-particle velocities observed at spot A would decrease significantly (Figure 9).

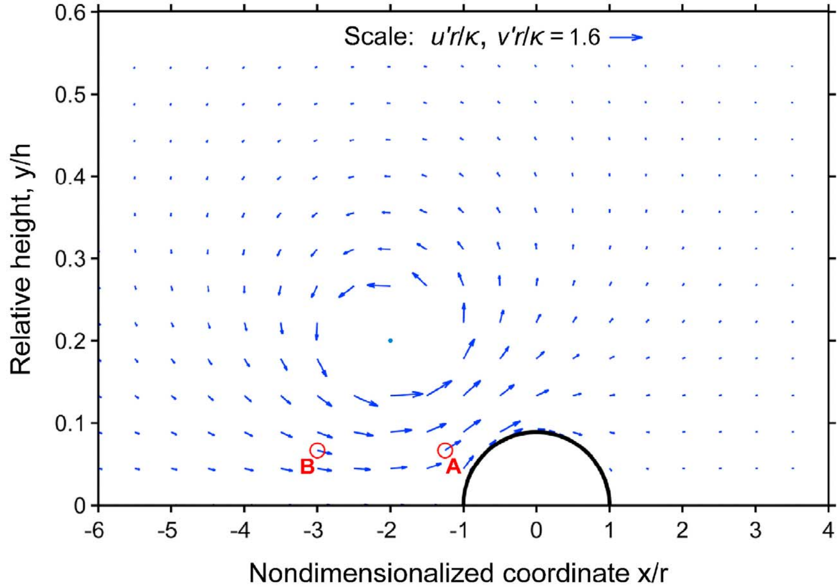

Figure 12. Vortex-induced coherent motion field (in z-plane) determined from the theoretical solution of the 2-D potential flow shown in Figure 9. Vortex is located at $(-2r, 0.2\,h)$; velocities are presented in non-dimensionalized forms ($u'r/\kappa$, $v'r/\kappa$). The velocity vector detected at the near-particle spot A differs from that detected at spot B located $1D$ upstream of the target particle.

[39] Second, the theoretical prediction shown in Figure 13b is compared with the velocities observed at spot B during particle entrainment (Run 2, e = 17 mm) [*Dwivedi et al.*, 2010]. We analyzed their time series of (u', v') using the shifted-time cumulative quadrant fraction approach. The result is shown in Figure 14, where a quadrant signature in agreement with the predicted variation sequence during the passage of a retrograde vortex is demonstrated. It is shown in Figure 14 that the pre-entrainment dominance of the Q1 fraction was replaced by that of the Q4 fraction at $\tau \approx -0.7$ s, followed by a continuous increase and a post-entrainment maximum of the Q4 fraction (>90%) at $\tau \approx 0.2$ s. The experimental result (Figure 14) appears to resemble the theoretical prediction (Figure 13b) in two aspects. (1) The pre-entrainment quadrant signature observed at spot B follows a sequence of variation where the dominance of Q1 is replaced by that of Q4. (2) The quadrant signature observed at spot B during the process of particle entrainment is dominated by Q4.

4.3. Quadrant Signatures Observed Under Different Pocket Geometries

[40] To reveal the quadrant signature that would be detected at the near-particle spot during entrainment of the target particle from a different type of pocket geometry, we performed another set of experiments (Set 3) including 210 full entrainment events (Table 1), in which the target particle was initially set in pocket 2 (Figure 3). The target particle was entrained from the diagonal valleys downstream of pocket 2 in directions at 60° with the velocity measurement plane. Figure 15 presents the pre- and post-entrainment cumulative quadrant fractions obtained based on an ensemble of all data from Set 3, where the pre-entrainment quadrant signature exhibits a variation pattern similar to those shown in Figure 9, while the post-entrainment quadrant signature demonstrates a variation pattern totally different from those seen in Figure 9. That is, the post-entrainment quadrant structure is dominated by Q2 instead of Q4; the post-entrainment Q3 fraction outperforms its Q1 counterpart, in contrast to the smallest Q3 fraction shown in Figure 9. As the post-entrainment cumulative quadrant fractions resume the long-term structure in background turbulence, the Q2 and Q3 fractions exhibit cumulative declining trends while the Q4 and Q1 fractions exhibit cumulative rising trends, as opposed to the corresponding cumulative trends observed in Figure 9.

[41] The similar pre-entrainment quadrant signatures observed in Sets 1∼3 and the reverse post-entrainment quadrant signature observed in Set 3, in particular the post-entrainment short-term dominance of Q2, imply that a retrograde-vortex-type coherent structure may have passed the measurement spot during particle entrainment. Such a structure, however, may have been obliquely oriented that is favorable to the particle entrainment in diagonal directions (Figure 3). Specifically, the structure orientation in the streamwise-transverse (x-z) plane may have been misaligned with the mean flow direction (LDV measurement plane). Such kind of misalignment is not unusual, since meandering has been noted as a feature of the near-bed coherent structures. For example, lately *Dennis and Nickels* [2011] made 3-D PIV measurements to demonstrate evidence of meandering hairpin packets observed earlier by *Hutchins and Marusic* [2007] using a spanwise rake of 10 hot-wires.

[42] The post-entrainment short-term dominance of the Q2 fraction uniquely observed in Set 3 also suggests that some of the reported contributions of Q2 in particle entrainment may have resulted from situations where the velocities were measured in a streamwise-vertical plane, but the target particle was set in a pocket geometry where it would tend to be entrained in diagonal directions by an obliquely oriented

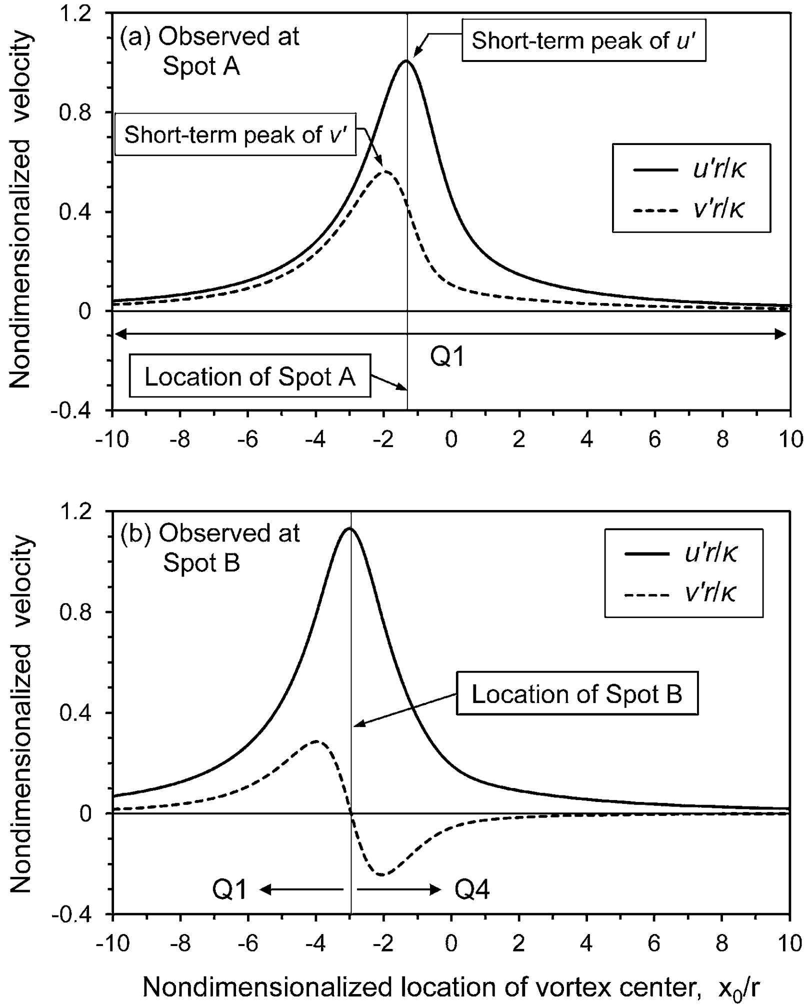

Figure 13. Nondimensionalized velocity components observed at (a) spot A, and (b) spot B as the vortex advances from the upstream to downstream of the target particle ($x_0 = -10\ r$ to $10\ r$). With the target particle remaining stationary, Q1 (outward interactions) is the vortex-induced quadrant signature that would be observed at spot A, the peak magnitude of u' is $\sim$ twice that of v', and the peak of u' lags behind that of v' by a small distance ($\approx r$). At spot B, Q1 is observed when the vortex is located upstream, but then Q4 (sweeps) is detected as the vortex moves to a location downstream of spot B; the vortex-induced quadrant signature observed at the time of entrainment is dominated by Q4.

structure that was misaligned with the measurement plane. Our results thus point to the potential discrepancy in the observed quadrant signatures that may arise from the heterogeneity of particle geometry.

5. Conclusions

[43] We conducted an experimental study to test the hypothesis that particle entrainment is associated with the passage of a retrograde vortex. The pre- and post-entrainment quadrant structures were probed with the LDV at a near-particle spot using the proposed shifted-time cumulative fraction approach. The results are characterized by a pre-entrainment spiky rise of the Q1 fraction and a mild increase of the Q4 fraction, followed by the post-entrainment dominance of the Q4 fraction and a drastic drop of the Q1 fraction. Such results imply that it is highly probable that particle entrainment is a result of the interactions with a passing retrograde-vortex-type coherent structure. Careful examinations of the results suggest that the quadrant signatures observed at the near-particle spot may have been influenced by the presence of the target particle in front of the measurement spot. However, it is still those short-term coherent structures that are associated with particle entrainment.

[44] Our results corroborate the previous observations that particle entrainment is primarily governed by sweeps (Q4) and outward interactions (Q1) [*Thorne et al.*, 1989; *Nelson et al.*, 1995; *Sterk et al.*, 1998; *Weaver and Wiggs*, 2008]. Even the fact that outward interactions (Q1) appear to be particularly efficient at producing entrainment [*Nelson et al.*, 1995, 2001] is suggested by our results. We established here in a more direct manner that two events of opposite sense of stress (i.e., Q1 and Q4) are the most important for particle entrainment, indicating that Reynolds stress may not be a good predictor of sediment transport. Although stress is of great value in an averaged sense, if we seek to make

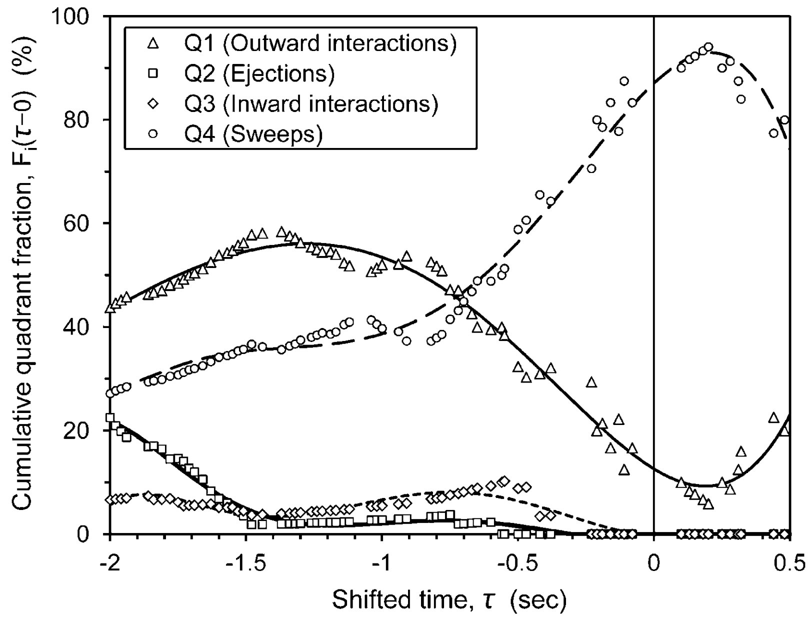

Figure 14. Pre- and post-entrainment cumulative quadrant fractions $F_i(\tau - 0)$ versus the shifted time τ, based on the time series of velocity data observed at spot B during particle entrainment [*Dwivedi et al.*, 2010]. The quadrant signature observed at spot B exhibits a sequence of variation where the pre-entrainment dominant Q1 fraction is replaced by the Q4 fraction, followed by a persistent rise and post-entrainment peak of the Q4 fraction. The best fit curves were obtained by using the fifth-degree polynomials.

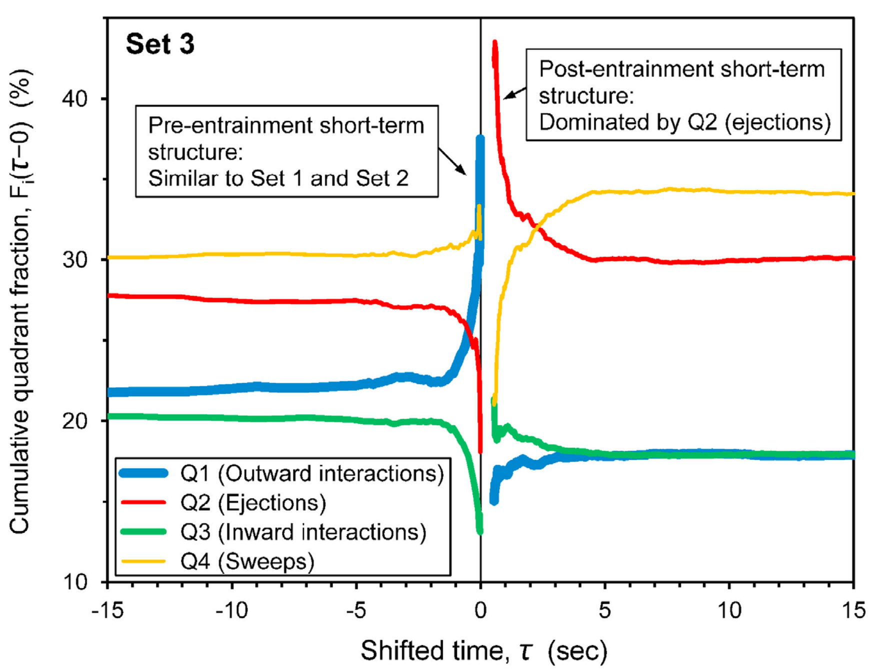

Figure 15. Pre- and post-entrainment cumulative quadrant fractions $F_i(\tau - 0)$ versus shifted time τ, based on an ensemble of all data from Set 3, in which the target particle was initially set in pocket 2. The pre-entrainment quadrant signature is similar to those shown in Figure 9, while the post-entrainment quadrant signature is completely different from those shown in Figure 9. The post-entrainment short-term structure is dominated by Q2 (ejections) rather than Q4 (sweeps). The post-entrainment Q2 and Q3 fractions exhibit cumulative declining trends, while the post-entrainment Q4 and Q1 fractions exhibit cumulative rising trends.

predictions of entrainment and transport in a high-frequency sense, we need to explore the problem in more detail.

[45] We also used a potential flow model to explore the quadrant signatures that would be observed at different locations during the passage of a retrograde vortex. The time series of 2-D velocities observed at the near-particle spot exhibit consistently the short-term peaks present at the time of entrainment. On the other hand, the quadrant signature observed at an alternative spot $1D$ upstream of the target particle exhibits a sequence of variation in which the pre-entrainment dominance of the Q1 fraction is replaced by that of the Q4 fraction, followed by a persistent rise and a post-entrainment peak of the Q4 fraction. These observations confirm the theoretical predictions, and demonstrate the difference in the quadrant signatures that would be observed at different locations during the process of particle entrainment.

[46] We performed an extra set of experiments where the target particle was set in pocket 2. The similar pre-entrainment quadrant signatures observed in experiments performed with different pocket geometries and the unique post-entrainment quadrant signature observed in the experiments using pocket 2, in particular the post-entrainment short-term dominance of the Q2 fraction, imply that an obliquely oriented retrograde-vortex-type coherent structure may have passed and entrained the target particle in diagonal directions. The results point to the potential discrepancy in the observed quadrant signatures arising from the misalignment of the velocity measurement plane with the direction of particle entrainment.

[47] The results presented here strongly suggest that particle entrainment is associated with the passage of a retrograde-vortex-type coherent structure. However, direct evidence of such structure or visualization of flow-particle interactions is not shown in the present work. This highlights the limitation of single-point LDV measurements and calls for the coupling of PIV and near-particle LDV observations in the future studies.

Notation

a	distance of vortex above X-axis (in Z-plane)
C	velocity distribution coefficient
D	diameter of the roughness elements
D_p	diameter of the target particle
$F_i\,(\tau - 0)$	shifted-time cumulative quadrant fractions focused at $\tau = 0$
$F_i\,(\tau - \tau_0)$	shifted-time cumulative quadrant fractions focused at a time point τ_0
Fr	Froude number $(=\bar{U}/\sqrt{gh})$
g	gravitational acceleration
H	hole size of threshold quadrant technique
h	flow depth
k	von Kármán constant (=0.4)
k_s	roughness height (=D)
k_s^+	roughness Reynolds number $(=u_* k_s/v)$
$N_i\,(\tau - \tau_0)$	number of ith-quadrant events in the time period $(\tau - \tau_0)$
Q_i	threshold quadrant fractions (i = 1, 2, 3, 4, 5)
r	radius of the target particle
Re	Reynolds number $(=\bar{U}h/\nu)$
s	specific gravity of the target particle
t	arbitrary time
t_E	initial time of particle entrainment
$\bar{U}$	depth-averaged mean streamwise velocity
(u, v)	streamwise and vertical components of local instantaneous velocity
$(\bar{u}, \bar{v})$	streamwise and vertical components of local mean velocity
(u', v')	streamwise and vertical velocity fluctuations = $(u - \bar{u}, v - \bar{v})$
$u'r/\kappa$, $v'r/\kappa$	nondimensionalized forms of u' and v'
(u_p, v_p)	near-particle streamwise and vertical instantaneous velocities
$(\bar{u}_p, \bar{v}_p)$	near-particle streamwise and vertical mean velocities
(u'_p, v'_p)	near-particle velocity fluctuations = $\left(u_p - \bar{u}_p, v_p - \bar{v}_p\right)$
u_*	bed shear velocity $(=\sqrt{\tau_b/\rho})$
V_a	mean advection velocity of background turbulent flow
V_c	vortex convection velocity in superimposed flowfield $(=V_a + V_s)$
V_s	self-induced speed of vortex (in coherent motion field)
w	complex potential of 2-D potential flow $(=\phi + i\psi)$
(x, y)	streamwise and vertical coordinates
y_*	viscous length scale $(=\nu/u_*)$
z, Z	complex variables, $z = x + iy$, and $Z = X + iY$
z_0, Z_0	vortex center in the z- and Z-plane, $z_0 = (x_0, y_0)$, and $Z_0 = (X_0, Y_0)$
$\bar{Z}_0$	complex conjugate of Z_0
δ	thickness of the linear (or roughness) layer
ϕ, ψ	velocity potential and stream function of 2-D potential flow
γ	normalized near-particle instantaneous Reynolds stress $(=\lvert u'_p v'_p\rvert/\sigma_{u,\,p}\sigma_{v,\,p})$
κ	vortex strength (in Z-plane)
ν	kinematic viscosity of water
θ	Shields stress $(=\tau_b/\rho g(s-1)D_p)$
θ_c	critical Shields stress
ρ	density of water
(σ_u, σ_v)	streamwise and vertical RMS turbulence intensities
$(\sigma_{u,p}, \sigma_{v,p})$	near-particle streamwise and vertical RMS turbulence intensities
τ	shifted-time variable $(=t - t_E)$
τ_0	point of interest in the shifted time frame
τ_b	bed shear stress
ω_z	spanwise vorticity in coherent motion field.

[48] **Acknowledgments.** This research was sponsored by the National Science Council, Taiwan, through the multiyear funding granted to F.-C. Wu (NSC 96-2628-E002-137-MY3, 94-2211-E002-037, 93-2211-E002-022). W.-R. Shih has been supported by a NSC special research assistantship (NSC 99-2221-E002-172-MY3). We thank Alex Pan for the LDV technical assistance. We are also grateful to Jon Nelson, two anonymous referees, and the Editors for insightful reviews that helped to improve this paper significantly.

References

Adrian, R. J. (2007), Hairpin vortex organization in wall turbulence, *Phys. Fluids*, *19*, 041301, doi:10.1063/1.2717527.

Adrian, R. J., C. D. Meinhart, and C. D. Tomkins (2000), Vortex organization in the outer region of the turbulent boundary layer, *J. Fluid Mech.*, *422*, 1–54, doi:10.1017/S0022112000001580.

Best, J. (1992), On the entrainment of sediment and initiation of bed defects: Insights from recent developments within turbulent boundary layer research, *Sedimentology*, *39*, 797–811, doi:10.1111/j.1365-3091.1992.tb02154.x.

Blackwelder, R. F., and R. E. Kaplan (1976), On the wall structure of the turbulent boundary layer, *J. Fluid Mech.*, *76*, 89–112, doi:10.1017/S0022112076003145.

Blanckaert, K., and H. J. de Vriend (2005), Turbulence structure in sharp open-channel bends, *J. Fluid Mech.*, *536*, 27–48, doi:10.1017/S0022112005004787.

Cameron, S. M. (2006), Near-boundary flow structure and particle entrainment, PhD thesis, Univ. of Auckland, New Zealand.

Christensen, K. T., and Y. Wu (2005), Visualization and characterization of small-scale spanwise vortices in turbulent channel flow, *J. Visualization*, *8*, 177–185, doi:10.1007/BF03181661.

Dennis, D. J. C., and T. B. Nickels (2011), Experimental measurement of large-scale three-dimensional structures in a turbulent boundary layer. Part 1. Vortex packets, *J. Fluid Mech.*, *673*, 180–217, doi:10.1017/S0022112010006324.

Detert, M., V. Nikora, and G. H. Jirka (2010), Synoptic velocity and pressure fields at the water-sediment interface of streambeds, *J. Fluid Mech.*, *660*, 55–86, doi:10.1017/S0022112010002545.

Dey, S., S. Sarkar, and F. Ballio (2011), Double-averaging turbulence characteristics in seeping rough-bed streams, *J. Geophys. Res.*, *116*, F03020, doi:10.1029/2010JF001832.

Diplas, P., C. L. Dancey, A. O. Celik, M. Valyrakis, K. Greer, and T. Akar (2008), The role of impulse on the initiation of particle movement under turbulent flow conditions, *Science*, *322*, 717–720, doi:10.1126/science.1158954.

Doligalski, T. L., C. R. Smith, and J. D. A. Walker (1994), Vortex interactions with walls, *Annu. Rev. Fluid Mech.*, *26*, 573–616, doi:10.1146/annurev.fl.26.010194.003041.

Dwivedi, A., B. W. Melville, and A. Y. Shamseldin (2010), Hydrodynamic forces generated on a spherical sediment particle during entrainment, *J. Hydraul. Eng.*, *136*, 756–769, doi:10.1061/(ASCE)HY.1943-7900.0000247.

Dwivedi, A., B. W. Melville, A. Y. Shamseldin, and T. K. Guha (2011), Flow structures and hydrodynamic force during sediment entrainment, *Water Resour. Res.*, *47*, W01509, doi:10.1029/2010WR009089.

Ferreira, R. M. L. (2011), Turbulent flow hydrodynamics and sediment transport: Laboratory research with LDA and PIV, in *Experimental Methods in Hydraulic Research*, *GeoPlanet: Earth and Planet. Sci.*, edited by P. Rowiński, pp. 67–112, Springer, Berlin.

Grass, A. J. (1970), Initial instability of fine sand, *J. Hydraul. Div. Am. Soc. Civ. Eng.*, *96*, 619–632.

Grass, A. J. (1971), Structural features of turbulent flow over smooth and rough boundaries, *J. Fluid Mech.*, *50*, 233–255, doi:10.1017/S0022112071002556.

Grass, A. J. (1974), Transport of fine sand on a flat bed: Turbulence and suspension mechanics, in *Euromech 48: Proceedings of the Colloquium on Transport, Erosion, and Deposition of Sediment in Turbulent Streams*, pp. 33–34, Inst. of Hydrodyn. and Hydraul. Eng., Tech. Univ. of Denmark, Lyngby.

Hardy, R. J., J. L. Best, S. N. Lane, and P. E. Carbonneau (2009), Coherent flow structures in a depth-limited flow over a gravel surface: The role of near-bed turbulence and influence of Reynolds number, *J. Geophys. Res.*, *114*, F01003, doi:10.1029/2007JF000970.

Hardy, R. J., J. L. Best, S. N. Lane, and P. E. Carbonneau (2010), Coherent flow structures in a depth-limited flow over a gravel surface: The influence of surface roughness, *J. Geophys. Res.*, *115*, F03006, doi:10.1029/2009JF001416.

Hardy, R. J., J. L. Best, D. R. Parsons, and G. M. Keevil (2011), On determining the geometric and kinematic characteristics of coherent flow structures over a gravel bed: A new approach using combined PLIF-PIV, *Earth Surf. Processes Landforms*, *36*, 279–284, doi:10.1002/esp.2118.

Hofland, B., and R. Booij (2004), Measuring the flow structures that initiate stone movement, in *River Flow 2004*, edited by M. Greco, A. Carravetta, and R. Della Morte, pp. 821–830, A. A. Balkema, Rotterdam, Netherlands.

Hurther, D., and U. Lemmin (2003), Turbulent particle flux and momentum flux statistics in suspension flow, *Water Resour. Res.*, *39*(5), 1139, doi:10.1029/2001WR001113.

Hussain, A. K. M. F. (1983), Coherent structures—Reality and myth, *Phys. Fluids*, *26*, 2816–2850, doi:10.1063/1.864048.

Hutchins, N., and I. Marusic (2007), Evidence of very long meandering features in the logarithmic region of turbulent boundary layers, *J. Fluid Mech.*, *579*, 1–28, doi:10.1017/S0022112006003946.

Kline, S. J., W. C. Reynolds, F. A. Schraub, and P. W. Runstadler (1967), The structure of turbulent boundary layers, *J. Fluid Mech.*, *30*, 741–773, doi:10.1017/S0022112067001740.

Lu, L. J., and C. R. Smith (1991), Use of flow visualization data to examine spatial- temporal velocity and burst-type characteristics in a turbulent boundary layer, *J. Fluid Mech.*, *232*, 303–340, doi:10.1017/S0022112091003701.

Lu, S. S., and W. W. Willmarth (1973), Measurements of the structure of the Reynolds stress in a turbulent boundary layer, *J. Fluid Mech.*, *60*, 481–511, doi:10.1017/S0022112073000315.

Mignot, E., D. Hurther, and E. Barthelemy (2009), On the structure of shear stress and turbulent kinetic energy flux across the roughness layer of a gravel-bed channel flow, *J. Fluid Mech.*, *638*, 423–452, doi:10.1017/S0022112009990772.

Milne-Thomson, L. M. (1968), *Theoretical Hydrodynamics*, 5th ed., Macmillan, London.

Nakagawa, H., and I. Nezu (1977), Prediction of the contributions to the Reynolds stress from bursting events in open-channel flows, *J. Fluid Mech.*, *80*, 99–128, doi:10.1017/S0022112077001554.

Natrajan, V. K., Y. Wu, and K. T. Christensen (2007), Spatial signatures of retrograde spanwise vortices in wall turbulence, *J. Fluid Mech.*, *574*, 155–167, doi:10.1017/S0022112006003788.

Nelson, J. M., R. L. Shreve, S. R. McLean, and T. G. Drake (1995), Role of near-bed turbulence structure in bed load transport and bed form mechanics, *Water Resour. Res.*, *31*, 2071–2086, doi:10.1029/95WR00976.

Nelson, J. M., M. W. Schmeeckle, and R. L. Shreve (2001), Turbulence and particle entrainment, in *Gravel-Bed Rivers V*, edited by M. P. Mosley, pp. 240–241, New Zealand Hydrol. Soc., Wellington, New Zealand.

Nezu, I., and H. Nakagawa (1993), *Turbulence in Open-Channel Flows*, A. A. Balkema, Rotterdam, Netherlands.

Nikora, V. (1999), Origin of the "-1" spectral law in wall-bound turbulence, *Phys. Rev. Lett.*, *83*, 734–736, doi:10.1103/PhysRevLett.83.734.

Nikora, V., and G. M. Smart (1997), Turbulence characteristics of New Zealand gravel-bed rivers, *J. Hydraul. Eng.*, *123*, 764–773, doi:10.1061/(ASCE)0733-9429(1997)123:9(764).

Nikora, V., D. Goring, I. McEwan, and G. Griffiths (2001), Spatially averaged open-channel flow over rough bed, *J. Hydraul. Eng.*, *127*, 123–133, doi:10.1061/(ASCE)0733-9429(2001)127:2(123).

Niño, Y., and M. H. Garcia (1996), Experiments on particle-turbulence interactions in the near-wall region of an open channel flow: Implications for sediment transport, *J. Fluid Mech.*, *326*, 285–319, doi:10.1017/S0022112096008324.

Pao, R. H. F. (1967), *Fluid Dynamics*, Merrill Books, Columbus, Ohio.

Parker, G. (2008), Transport of gravel and sediment mixtures, in *Sedimentation Engineering: Processes, Measurements, Modeling, and Practice*, edited by M. H. García, pp. 165–251, Am. Soc. Civ. Eng., Reston, Va.

Pope, S. B. (2000), *Turbulent Flows*, Cambridge Univ. Press, Cambridge, UK, doi:10.1017/CBO9780511840531.

Roy, A. G., T. Buffin-Bélanger, H. Lamarre, and A. D. Kirkbride (2004), Size, shape and dynamics of large-scale turbulent flow structures in a gravel-bed river, *J. Fluid Mech.*, *500*, 1–27, doi:10.1017/S0022112003006396.

Schmeeckle, M. W., J. M. Nelson, and R. L. Shreve (2007), Forces on stationary particles in near-bed turbulent flows, *J. Geophys. Res.*, *112*, F02003, doi:10.1029/2006JF000536.

Sechet, P., and B. le Guennec (1999), The role of near wall turbulent structures on sediment transport, *Water Res.*, *33*, 3646–3656, doi:10.1016/S0043-1354(99)00072-X.

Shvidchenko, A. B., and G. Pender (2001), Macroturbulent structure of open-channel flow over gravel beds, *Water Resour. Res.*, *37*, 709–719, doi:10.1029/2000WR900280.

Singh, A., F. Porte-Agel, and E. Foufoula-Georgiou (2010), On the influence of gravel bed dynamics on velocity power spectra, *Water Resour. Res.*, *46*, W04509, doi:10.1029/2009WR008190.

Smart, G. M. (2006), A novel gravel entrainment investigation, in *River, Coastal and Estuarine Morphodynamics: RCEM 2005*, edited by G. Parker and M. H. García, pp. 65–70, Taylor and Francis, London.

Smart, G. M., and H. M. Habersack (2007), Pressure fluctuations and gravel entrainment in rivers, *J. Hydraul. Res.*, *45*, 661–673, doi:10.1080/00221686.2007.9521802.

Smith, C. R., J. D. A. Walker, A. H. Haidari, and U. Sobrun (1991), On the dynamics of near-wall turbulence, *Philos. Trans. R. Soc. London, Ser. A*, *336*, 131–175, doi:10.1098/rsta.1991.0070.

Sterk, G., A. F. G. Jacobs, and J. H. van Boxel (1998), The effect of turbulent flow structures on saltation sand transport in the atmospheric boundary layer, *Earth Surf. Processes Landforms*, *23*, 877–887, doi:10.1002/(SICI)1096-9837(199810)23:10<877::AID-ESP905>3.0.CO;2-R.

Sumer, B. M., and R. Deigaard (1981), Particle motions near the bottom in turbulent flow in an open channel. Part 2, *J. Fluid Mech.*, *109*, 311–337, doi:10.1017/S0022112081001092.

Sutherland, A. J. (1967), Proposed mechanism for sediment entrainment by turbulent flows, *J. Geophys. Res.*, *72*, 6183–6194, doi:10.1029/JZ072i024p06183.

Thorne, P. D., J. J. Williams, and A. D. Heathershaw (1989), In situ acoustic measurements of marine gravel threshold and transport, *Sedimentology*, *36*, 61–74, doi:10.1111/j.1365-3091.1989.tb00820.x.

Valyrakis, M., P. Diplas, C. L. Dancey, K. Greer, and A. O. Celik (2010), Role of instantaneous force magnitude and duration on particle entrainment, *J. Geophys. Res.*, *115*, F02006, doi:10.1029/2008JF001247.

Voulgaris, G., and J. H. Trowbridge (1998), Evaluation of the acoustic Doppler velocimeter (ADV) for turbulence measurements, *J. Atmos. Oceanic Technol.*, *15*, 272–289, doi:10.1175/1520-0426(1998)015<0272:EOTADV>2.0.CO;2.

Wallace, J. M., H. Eckelman, and R. S. Brodkey (1972), The wall region of turbulent shear flow, *J. Fluid Mech.*, *54*, 39–48, doi:10.1017/S0022112072000515.

Wallace, J. M., R. S. Brodkey, and H. Eckelman (1977), Pattern-recognized structures in bounded turbulent shear flows, *J. Fluid Mech.*, *83*, 673–693, doi:10.1017/S0022112077001402.

Weaver, C. M., and G. F. S. Wiggs (2008), Sweeping up sand: Coherent flow structures and sediment entrainment, paper presented at European Geophysical Union 2008 General Assembly, Vienna.

Willmarth, W. W., and S. S. Lu (1972), Structure of the Reynolds stress near the wall, *J. Fluid Mech.*, *55*, 65–92, doi:10.1017/S002211207200165X.

Wu, F.-C., and Y.-J. Chou (2003), Rolling and lifting probabilities for sediment entrainment, *J. Hydraul. Eng.*, *129*, 110–119, doi:10.1061/(ASCE)0733-9429(2003)129:2(110).

Wu, F.-C., and M.-R. Jiang (2007), Numerical investigation of the role of turbulent bursting in sediment entrainment, *J. Hydraul. Eng.*, *133*, 329–334, doi:10.1061/(ASCE)0733-9429(2007)133:3(329).

Wu, Y., and K. T. Christensen (2006), Population trends of spanwise vortices in wall turbulence, *J. Fluid Mech.*, *568*, 55–76, doi:10.1017/S002211200600259X.